

Model-Based Error Correction for Instrument Flexion in Robotic Surgery

A thesis presented

by

Ryan Andrew Beasley

to

The Division of Engineering and Applied Sciences

in partial fulfillment of the requirements for the degree of

Doctor of Philosophy

in the subject of

Engineering Sciences

Harvard University

Cambridge, MA

August 17, 2006

Robert D. Howe**Ryan Andrew Beasley**

Thesis Advisor

Author

Model-Based Error Correction for Instrument Flexion in Robotic Surgery

Abstract

Surgical robots can improve the safety of minimally invasive surgeries through image guidance and motion filtering, but design choices that reduce patient trauma (e.g., thin instrument shafts) lead to intraoperative variation in kinematic parameters. The resulting kinematic errors can degrade image-guidance methods and cause instrument motions in undesired directions. This work addresses the most significant kinematic errors: quasi-static instrument shaft flexion and motion of the port through which the instrument is introduced into the patient.

First, a metric is presented to determine the impact of kinematic errors on instrument motions. The metric quantifies how closely an erroneous robot controller will move the instrument to its desired position in a single step, as well as the worst-case angular difference between desired motions and actual motions. Simulations and experiments demonstrate results for kinematic errors due to port motion. Uses for the measure include predicting monotonic convergence, path planning, and robot design.

Second, a model-based controller is proposed to correct the instrument motions. The controller models quasi-static instrument flexion and port motion as a pinned-pinned beam with a point load at the port. The proposed controller is evaluated using the above metric, for various instrument lengths, flexion, and sensor noise, and is compared with a controller assuming a straight instrument shaft. Through 2D quasi-static simulations and experiments, the proposed controller's motion errors are shown to be half the size of errors for the straight shaft controller. Additionally, the ability to implement the model using various sensors is demonstrated in dynamic experiments using two different sensor modalities, electromagnetic position/orientation sensors compared with strain gage force sensors.

Third, the benefits of more accurate kinematics are compared relative to the benefits from directly measuring the instrument tip's position. Four controllers are developed, two with the proposed flexion kinematic model and two with tip tracking. A user study determines the performance of these four controllers in a 3D image guided teleoperation task involving instrument shaft flexion. Using either improved kinematics or tip tracking reduces motion errors compared with the current standard controller, but the best performance is with the proposed controller, which uses both enhancements.

Contents

| | |
|--|-----|
| Abstract | iii |
| Contents | v |
| Acknowledgements | vii |
| Chapter 1 Introduction | 1 |
| 1.1 Kinematic errors | 2 |
| 1.2 Previous Research | 4 |
| 1.3 Overview of Thesis | 5 |
| Chapter 2 Metric for Motion Errors | 7 |
| 2.1 Introduction | 7 |
| 2.2 Analysis of Controller | 8 |
| 2.3 Examples | 13 |
| 2.4 Discussion | 20 |
| Chapter 3 Model-Based Error Correction for Flexible Instruments | 24 |
| 3.1 Introduction | 24 |
| 3.2 Controller Design | 24 |
| 3.3 Controller Evaluation | 30 |
| 3.4 Results | 31 |
| 3.5 Discussion | 34 |
| Chapter 4 Experimental Validation in Two Dimensions | 38 |
| 4.1 Introduction | 38 |
| 4.2 Calculating Model Parameters | 38 |
| 4.3 Methods | 40 |
| 4.4 Results | 43 |
| 4.5 Discussion | 44 |
| Chapter 5 3D Image-Guided Teleoperation User Study | 48 |
| 5.1 Introduction | 48 |

| | |
|---|----|
| 5.2 Methods | 49 |
| 5.3 Results | 59 |
| 5.4 Discussion | 62 |
| Chapter 6 Conclusions and Future Work | 66 |
| 6.1 Evaluation of Motion Errors | 66 |
| 6.2 Image-guidance benefits from tip tracking | 67 |
| 6.3 Kinematic modeling | 68 |
| 6.4 Future Work | 69 |
| References | 72 |

Acknowledgements

Throughout this work, I have been well assisted by my thesis committee, Professors Robert Howe, Roger Brockett, and Pierre Dupont. I have left each and every meeting with my advisors feeling more enlightened as a result of their many insightful questions urging me to understand the larger picture of my work and my future. Professor Howe, in particular, has taught me a significant amount about engineering research. By his suggestion I started this research path, and guided by our regular meetings I have finished it.

As an undergraduate, I learned how enjoyable engineering research can be from Professor Robert Galloway Jr. I fondly remember the time spent working in his lab. His words of encouragement during my graduate career have been much appreciated.

My labmates have provided specialist knowledge, research ideas, critical suggestions, and their time. I dread to imagine how lonely graduate school would have been without them. Thanks go to Douglas Perrin, Marius Linguraru, Heather Gunter, Anna Galea, Sol Diamond, Amy Kerdok, Aaron Dollar, Paul Novotny, Petr Jordan, Yuri Ishihara, and Shelten Yuen, as well as all of the undergraduates and visiting students that spent time with us. A special thanks goes to labmate Chris Wagner. Chris taught me the most important lesson I learned during graduate school: new ideas and side projects are to be pursued. No idea is impossible, and we can probably have the experiment done and the paper written within the week. Don't procrastinate, don't prematurely optimize, and

certainly don't delay for tasks already on your plate. None of it would have been any fun without Chris.

My family has always believed in me, no matter the difficulty of my task or the glacial progress. You made me who I am today. Thank you.

No words seem powerful enough to describe how important Professor Joanna Lahey, my wife, has been to the completion of this work. I would not have succeeded without her unconditional support, editing prowess, and her example of what it takes to graduate. I consider myself lucky just to have her as my friend.

Chapter 1

Introduction

In robotic surgery, the surgical instruments are manipulated by robots, either autonomously or commanded by a surgeon. From accurate kinematic models of the robot arm, the instrument tip's current position can be calculated, along with arm geometries to place the tip at desired positions. With these two capabilities, robots provide surgeons with at least three advantages: instrument motion filtering, intuitive controls, and enhanced image-guidance. These advantages can improve patient safety and are most desired for difficult minimally invasive surgeries (MIS).

In MIS, the surgical site is accessed using long-handled instruments passed through small incisions (~1 cm long). Observation of the surgical site is accomplished with a camera passed through another small incision. The small incisions lessen trauma to healthy tissue compared with traditional procedures and result in correspondingly shorter hospital stays. The downside of MIS is increased surgical difficulty due to degraded visual feedback, reduced tactile information, and a complicated mapping between hand motions and motions of the instrument tip.

To reduce this surgical difficulty, robots can assist in controlling the instruments. Tip positioning precision is increased by filtering out hand tremor and by scaling large hand

motions down to smaller instrument motions [Hills 98] [Panait 02] [Guthart 00]. Surgical robots also provide intuitive interfaces. Instrument tip motions can directly mimic the surgeon's hand motions, and for instruments that have wrists inside the patient, the orientation of the surgeon's hands can be used to orient those wrists [Falk 99].

Image-guidance techniques provide additional assistance to the surgeon. First, since the instrument's position can be calculated from the kinematics, that position can be displayed directly on pre-operative medical images [Grimson 98] [Peters 00]. Similarly, elements from the medical images can be overlaid on the camera's view. Such augmented reality improves tool navigation and the surgeon's mental model of the surgical environment. Second, the robot can actively guide the instrument towards, or away from, specific locations in the images by using virtual fixtures [Park 01] [Abbott 03] [Marayong 03]. One type of virtual fixture exerts forces against the surgeon's hands to provide navigational information. Another type constrains the instrument position to a specific area, protecting delicate anatomy around that area. Regardless of the specifics, image-guidance techniques such as virtual fixtures and augmented reality provide navigational benefits by combining medical images with the capabilities of a robot.

1.1. Kinematic errors

These benefits from surgical robots are dependent on accurate kinematic models. Under inaccurate kinematics, the desired instrument motions may be filtered, but the actual motions can be in undesired directions. The instrument wrist's orientation may be simple to control, but not mimic the orientation of the surgeon's hand. The instrument position, calculated from erroneous kinematics and displayed on medical images, does not correspond to the actual location of the instrument. Similarly, virtual fixtures will

behave improperly by allowing the instrument to reach into forbidden regions, because of incorrect tip position calculations or erroneous calculation of the desired arm geometry.

Minimally invasive surgical robots suffer from kinematic errors due to incorrect estimates of the port position, inaccurate assumptions of the instrument shaft's shape, compliance in the joints and links, and backlash and friction in the actuators. The first two of these errors arise from the constraints of MIS. The port position is important as it is the fulcrum relating the robot's motions to the corresponding motions of the instrument tip. Patient motions, such as breathing, can displace the port from its estimated position. Furthermore, forces from the instrument tip interacting with the surgical site can cause reaction forces that displace the port. These tip forces can also cause the thin instrument to flex, thereby invalidating the standard assumption of a straight instrument. For example, applying 1 N to the tip of a cantilevered instrument for a commercial surgical robot results in a 15 mm tip deflection (endoscissors, ZEUS Surgical Robot System, Computer Motion, Inc; Goleta, Calif.).

To ensure the benefits of robotic surgery, either such changes need to be mechanically prevented, or the kinematic models need to adjust to the physical changes. Compliance in joints and links can be reduced with stiffer components. Similarly, more precise actuators would reduce the backlash and friction. Design choices that would limit port motion and instrument flexion include thicker instruments made from stiffer materials, guide tubes that surround the instrument portion outside of the patient, and a support to hold the port position constant. Such choices would constrain the kinematic changes in MIS, but at the expense of increased invasiveness, mechanical complexity, and higher material costs. Alternatively, these factors can be minimized if the surgical

robot system is robust to changing kinematics. This work follows the latter approach by improving the control of the robot to reduce the effects of kinematic errors on instrument motions and the estimated tip position.

1.2 Previous Research

Previous research has developed two approaches to kinematic errors: measuring the tip position and improving the kinematic model. The tip position calculation can be bypassed by directly measuring the position, for example using computer vision techniques or electromagnetic sensors [Hutchinson 96]. Such measurements solve part of the problem caused by invalid kinematics, but do not improve the calculation of arm geometries that move the instrument to desired positions. Therefore, position measurements improve the accuracy of augmented reality, but the instrument will still move in undesired directions. Metrics have been developed that evaluate whether controllers that utilize tip tracking will drive the tip to the desired position, but the metrics do not determine how much the trajectory will deviate from the desired path and do not reduce the motion errors [Cheah 03].

Previous work on improving the kinematic model includes calibration, Uncalibrated Visual Servoing (UVS), and flexible manipulator modeling. Calibration attempts to accurately determine kinematic parameters. One of the most popular calibration methods consists of constraining the robot endpoint to a position or surface and then exercising any degrees of freedom in the resulting kinematic chain [Hollerbach 96], [Roth 87]. Similarly, an external measurement system (e.g., computer vision) can track the robot endpoint, thereby closing the kinematic chain without constraining the robot. Since such methods are performed pre-operatively, they do not address the kinematic changes of

interest, which are caused by interaction between the instrument and the unmodeled environment.

Similar to calibration, UVS models the relationship between the measured endpoint motion and motions of the robot's actuators [Hosoda 94] [Jägersand 96] [Piepmeier 99]. The model is updated after each motion and thus immediately adjusts to changing kinematics. The obstacle to using UVS in the control of surgical robots is that the model accuracy is dependent on regular motions in all directions, a prohibitive task in the surgical environment.

Flexible manipulator research has focused on how to accurately command tip motions when those motions cause the manipulator to dynamically flex [Rovner 87], [Kwon 94]. That research relies on knowing the static kinematics and determining the flexible modes of the manipulator. Dynamic flexion is negligible in robotic surgery because the motions are slow and the instruments are in contact with a viscoelastic environment [Fung 93]. The resulting flexion is quasi-static and has not been previously addressed in flexible structures research.

1.3 Overview of Thesis

The presented work investigates the impact of erroneous kinematics in image-guided robotic surgery, and proposes a controller to reduce that impact. In chapter 2, a metric is developed to quantify the effects of kinematics errors. Given the true kinematics and the incorrect kinematic model, the metric determines the worst case motion error that can result. In chapter 3, a model-based controller is presented that accounts for kinematic changes due to instrument shaft flexion and port motion. The metric from the previous chapter is used to evaluate the controller's performance as a function of instrument

lengths and tip forces, and in the presence of sensor noise. Chapter 4 examines two-dimensional simulation and experimental results for quasi-static motions made using the proposed controller and the standard controller. Along with those comparisons are dynamic results that illustrate the potential motion errors for erroneous kinematics and long desired motions. Chapter 5 describes a user study using a teleoperated robot system to explore the separate benefits to image-guided robotic surgery from tracking the instrument tip's position and employing the proposed kinematic model. The results show that the combination of tip tracking and the proposed model prevents most of the positioning errors caused by instrument flexion. Topics for continued research are discussed in the final chapter.

Chapter 2

Metric for Motion Errors

2.1. Introduction

Minimally invasive surgery (MIS) uses long instruments inserted through small ports in the patient's body. This technique greatly reduces patient trauma but increases surgical difficulty due to decreased dexterity and restriction of visual, tactile, and proprioceptive feedback. Robot assistance can help offset such complications by providing instrument localization, image guidance, navigational tools (e.g., virtual fixtures), dampening of hand tremor, and workspace scaling. Unfortunately, laboratory and clinical trials demonstrate that errors in the robotic system result from uncertain kinematics, unmodeled dynamics, and unmodeled forces [Coste-Maniere 04]. Internal mammary artery takedown is an example task that exhibits such errors [Park 01]. To reach the surgical site near the chest wall, the instrument shaft applies significant torque to the port. The moments and forces created during the operation cause the patient's ribs to flex, the port to move, and the instrument shaft to bend. These kinematic errors impair positioning of the robot and cause deviations from the desired motions. Reducing the positioning precision reduces the navigational benefits of the robot. In the worst case, the robot may move the instrument in undesired directions, decreasing patient safety.

For robots using an inverse Jacobian controller, this chapter presents a measure of the positioning error in the controller based on the error in the Jacobian. That measure can be used to determine whether the system is monotonically convergent, and to estimate the maximum angular difference between desired motions and actual motions as produced by the controller. The maximum angular difference can then be used to determine how closely the system would follow commanded motions. Simulations and experimental data are used to illustrate the measure for a laboratory robot system. Practical uses for the measure are then discussed such as predicting monotonic convergence, path planning, and robot design.

2.2. Analysis of Controller

An ideal robotic system moves to the commanded position and follows a straight path to that position. The first trait translates to asymptotic convergence and the second trait is related to monotonic convergence. For design and safety reasons, it is important to have a measure of the effect that errors in the controller have on these properties of the system. The measure developed here uses a quasi-static assumption to calculate both the Cartesian error length after a motion and the angle between desired and actual motions.

2.2.1. Controller and Assumptions

In image-guided robotic surgery, the robot holds onto the surgical instruments. As in many laparoscopic and thoracoscopic procedures, it is assumed that the surgical instruments are introduced into the patient's body through *endoscopic ports*, rigid cannulae a few cm in length that are tightly inserted into small incisions. In addition to the instruments, a *laparoscope* is inserted into the patient to provide visual feedback. The surgeon observes the laparoscopic image and establishes the desired instrument positions

by manipulating handles at the surgeon's console. The robot positions the instruments in a world coordinate frame using motor torques commanded by the controller.

Focusing on surgical robots influences the choice of feedback controllers. The proposed controller will augment an existing surgical robot, with a built-in joint-level controller. That joint-level controller runs with a high servo rate and has critically damped or over-damped behavior, with properties set at initial design. Additionally, the joint-level controller has regulatory approval requiring thousands of surgical cases, which inhibits modifications.

The joint level controller accepts a set of desired joint angles, calculated using the Jacobian relating changes in the angles to changes in the robot's position. Jacobian based controllers are appealing because, when combined with measurements of the robot position, the system converges to the desired position even in the presence of small kinematic errors. Combining the Jacobian with the existing controller (Fig. 2.1), the desired position for the robot can be set and the robot will move to that position, barring significant kinematic errors.

While contacts between the instrument shaft and the environment can introduce kinematic errors, these contacts have the benefit of reducing the effects of system dynamics. The contacts increase the damping of the system, leading to a quasi-static

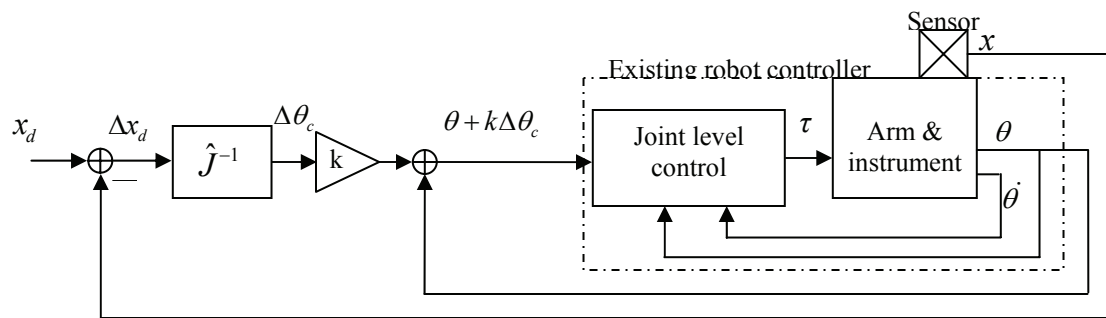


Figure 2.1. Block diagram of controller.

situation. Critically damped joint-level control also leads to a quasi-static situation due to its minimum settling time and no overshoot. With these features, a quasi-static assumption holds as long as the commanded angular changes are small enough to be completed before the next update of the inverse Jacobian controller. To satisfy this constraint, the motion scaling gain of the controller may be decreased until the system behaves in a quasi-static manner.

2.2.2. Derivation of Error Measures

For an inverse Jacobian controller with an imperfect Jacobian, the commanded change in joint angles, $\Delta\theta_c \in \mathbb{R}^n$ where n is the degrees of freedom for the robot, is calculated as

$$\Delta\theta_c = k\hat{J}^{-1}(x_d - x) = k\hat{J}^{-1}\Delta x_d, \quad (2.1)$$

where $x \in \mathbb{R}^3$ is the current Cartesian position, $x_d \in \mathbb{R}^3$ is the desired position in Cartesian space, \hat{J} is an estimate of J , the true system Jacobian, and k is a motion scaling gain. For infinitesimal steps and an ideal quasi-static system, the resulting motion is

$$\Delta x = J\Delta\theta_c = kJ\hat{J}^{-1}\Delta x_d. \quad (2.2)$$

Therefore the new position after completing the motion is (Fig. 2.2)

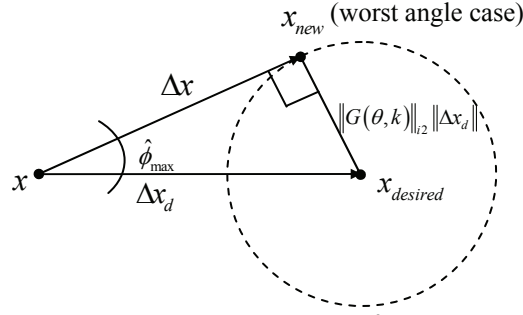
$$x_{new} = \Delta x + x = kJ\hat{J}^{-1}\Delta x_d + x, \quad (2.3)$$

and the error after completing the motion is

$$\Delta x_{new} = x_d - x_{new} = x_d - x - kJ\hat{J}^{-1}\Delta x_d. \quad (2.4)$$

A mapping, $G(\theta, k)$, is defined from Δx_d to Δx_{new} .

$$\Delta x_{new} = G(\theta, k)\Delta x_d = (I - kJ\hat{J}^{-1})\Delta x_d. \quad (2.5)$$

Figure 2.2. Geometry of $\hat{\phi}_{\max}$.

To analyze convergence, the induced Euclidean norm of $G(\theta, k)$ can be defined in the standard way

$$\|G(\theta, k)\|_{i_2} = \max_{\Delta x_d \neq 0} \frac{\|G\Delta x_d\|_2}{\|\Delta x_d\|_2} = \bar{\sigma}(G), \quad (2.6)$$

where $\bar{\sigma}(G)$ denotes the maximum singular value of G . If $\|G(\theta, k)\|_{i_2} < 1, \forall \theta$, the Cartesian error length is always smaller after a step than before the step. Therefore, the Cartesian error length monotonically decreases to zero with subsequent steps, making the controller monotonically and asymptotically convergent. Let v_σ be the right singular vector that corresponds to the maximum singular value, $\bar{\sigma}(G)$. Note that v_σ is the desired direction that results in the largest $\|\Delta x_{new}\|$. Also note, neither $\|G(\theta, k)\|_{i_2}$ nor v_σ have any application to the orientation of the robot.

While $\|G(\theta, k)\|_{i_2}$ is useful, a potentially more important measure is the angle, ϕ , between the desired motion, Δx_d , and the actual motion, Δx (Fig. 2.2). If $|\phi|$ is small for all possible motions across the workspace, then for a teleoperated system the slave robot will accurately follow the motions of the master. Let $|\phi_{\max}(\theta)|$ be the maximum absolute

value of ϕ over all desired motions, for a specific joint configuration, θ . From the definition of singular value decomposition,

$$Gv_i = \sigma_i u_i, \quad (2.7)$$

where v_i are the right singular vectors of G , u_i are the left singular vectors of G , and σ_i are the corresponding singular values. So pairs of input and output vectors can be defined where the input vectors, \bar{v} , are unit length,

$$\left(\bar{v} = \sum_{i=1}^m \alpha_i v_i, \sum_{i=1}^m \alpha_i^2 = 1 \right) \xrightarrow{G} \left(\bar{u} = \sum_{i=1}^m \sigma_i \alpha_i u_i \right), \quad (2.8)$$

where $m = \dim(x)$. Then

$$|\phi_{\max}(\theta)| = \max_{\bar{v}} \left\{ \cos^{-1} \left(\frac{\bar{v}^T (\bar{v} - \bar{u})}{\|\bar{v} - \bar{u}\|_2} \right) \right\}. \quad (2.9)$$

Equation (2.9) calculates the exact value of $|\phi_{\max}(\theta)|$, but requires searching over a sphere of radius 1, invoking computational requirements tolerable for offline calculations but that may be too great for real-time use. Instead, an upper bound on $|\phi_{\max}(\theta)|$ can be determined geometrically from $\|G(\theta, k)\|_{i2}$. Note that x_{new} must lie within a sphere of radius $\|G(\theta, k)\|_{i2} \|\Delta x_d\|$ from x_d . The conservative estimate, $\hat{\phi}_{\max}(\theta, k)$, of $|\phi_{\max}(\theta)|$ is constructed by assuming the actual motion has the largest possible $|\phi|$. In that case, the actual motion is tangential to the surface of the sphere about x_d , putting a right angle between the actual motion and the radius of the sphere. The resulting right triangle has the desired motion as its hypotenuse. An upper bound on $\phi_{\max}(\theta)$ is therefore

$$\begin{aligned}\hat{\phi}_{\max}(\theta, k) &= \sin^{-1}\left(\frac{\|G(\theta, k)\|_{l_2} \|\Delta x_d\|}{\|\Delta x_d\|}\right) \\ &= \begin{cases} \sin^{-1}(\bar{\sigma}(G)) & , \bar{\sigma}(G) \leq 1 \\ \pi & , \bar{\sigma}(G) > 1. \end{cases}\end{aligned}\quad (2.10)$$

Let p_ϕ be the direction of desired motion that results in $|\phi_{\max}|$.

2.3. Examples

To demonstrate the various measures and variables, a simplified MIS robot system was simulated quasi-statically using the controller in Fig. 2.1. Kinematic errors due to displacement of the instrument port were introduced, and $|\phi_{\max}|$, $\|G(\theta, k)\|_{l_2}$, $\hat{\phi}_{\max}$, p_ϕ , and v_σ were calculated across the workspace of the system. This source of error was chosen for its ease of implementation and straightforward implications. The following chapter addresses kinematic errors due to instrument flexion. Additionally, an experimental setup used the same controller to generate trajectories for various initial and desired positions in the presence of kinematic errors. These trajectories were compared with simulation results.

2.3.1. Computer Simulation

The simulation consisted of a planar two-link robot attached to an instrument shaft. The workspace and configuration from the experiment were used for the simulation (Fig. 2.3). The workspace of the robot's wrist is broken into two classifications depending on whether the instrument shaft could reach the port with the robot at that position. The links were each 210 mm long and the instrument shaft was 320 mm long, to match the experimental setup described below. The home position was with the first link

horizontal (parallel to the z -axis) and the second link vertical (parallel to the y -axis). The origin was at the wrist of the robot in its home position. The instrument shaft passed through a port that was placed at $(y = 0, z = 160)$. We assume that the first joint is constrained to angular values between 1.2 and -1.9 radians as measured from the home position. The second joint is constrained to angular values between 1.0 and -0.7 radians as measured from the home position. Additionally, the joints are constrained such that the sum of the angles for both joints is between 2.8 and -0.3 radians. These joint constraints are similar to the physical constraints of the robot used in the experimental setup, described in the next section.

For each point in the tip workspace, the error metrics are calculated with a port positioning error of $+20$ mm in y and $+10$ mm in z , and assuming quasi-static steps (Fig. 2.4). The induced Euclidean norm, $\|G(\theta, 1)\|_{i_2}$, is greater than unity for a large portion of the workspace, so monotonic convergence is not guaranteed over the entire workspace.

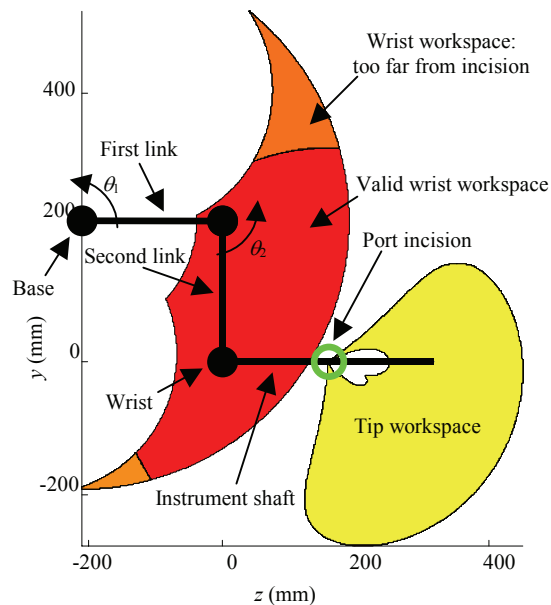


Figure 2.3. Diagram of wrist and tip workspaces, with links and shaft as lines and port as a circle.

However, $\|G(\theta, k)\|_{i_2} \leq 0.5$ in the middle of the workspace, so small desired motions there should be monotonically convergent. In general, as the controller gain, k , decreases from unit gain to zero, the commanded motions shrink in length and so $\|G(\theta, k)\|_{i_2}$ constricts to values closer to 1. As $k > 1$, $\|G(\theta, k)\|_{i_2}$ increases proportionally, due to the larger motions. The regions signified by the points L , M , and N in Fig. 2.4 were used in the experimental tests.

Fig. 2.4b shows the estimate, $\hat{\phi}_{\max}(\theta, k)$ with unit gain. The latter two plots demonstrate that $\hat{\phi}_{\max}$ is a conservative estimate of $|\phi_{\max}|$. In fact, the contour line at the right of the workspace, beyond which $\hat{\phi}_{\max}$ is greater than 135 degrees, approximately corresponds to where $|\phi_{\max}|$ is greater than 45 degrees. Examining $|\phi_{\max}|$, the actual motion is within 90 degrees of the desired motion for most of the workspace. In all three plots, larger values occurred when either the robot or the shaft tip were near the port position, locations at which the effects of the port's position error on the controller are greatest.

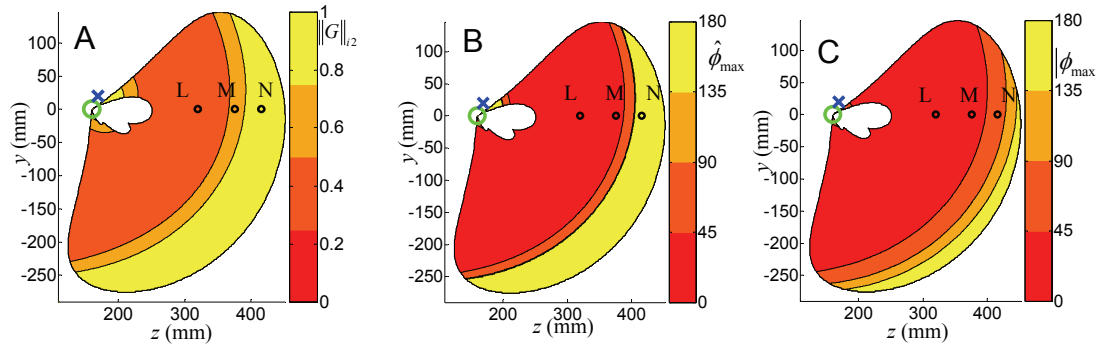


Figure 2.4. (A) $\|G\|_{i_2}$, (B) $\hat{\phi}_{\max}$ (degrees), and (C) $|\phi_{\max}|$ (degrees) for port positioning error of (20, 10) mm. The circle shows the true port location. The 'x' is the estimated port location.

A vector plot of v_σ displays the desired motion directions that maximized $\|\Delta x_{new}\|$, the Cartesian error lengths after the actual motions (Fig. 2.5). Of interest are the locations where nearby vector lines are perpendicular to each other, because at those locations small changes of position cause large changes in v , such as in the lower left corner and around the port. Except in the lower left corner, the v_σ for positions along the edge of the workspace are all approximately perpendicular to the boundary of the workspace. Scaling the same line segments by $\|G(\theta, k)\|_{i2}$, shows that even though v changes direction rapidly in the center of the workspace the errors there are not significant. A vector plot of p_ϕ , the directions of desired motions that result in the maximum angular error, is similar to the plot for v_σ , but differences exist in the bottom left and along the edge of the workspace. Also, p_ϕ seems to change more smoothly than v_σ around the left-center of the workspace. Scaling the same plot by the maximum angular error emphasizes the difference between v and p_ϕ around the workspace boundary, where motion errors are largest.

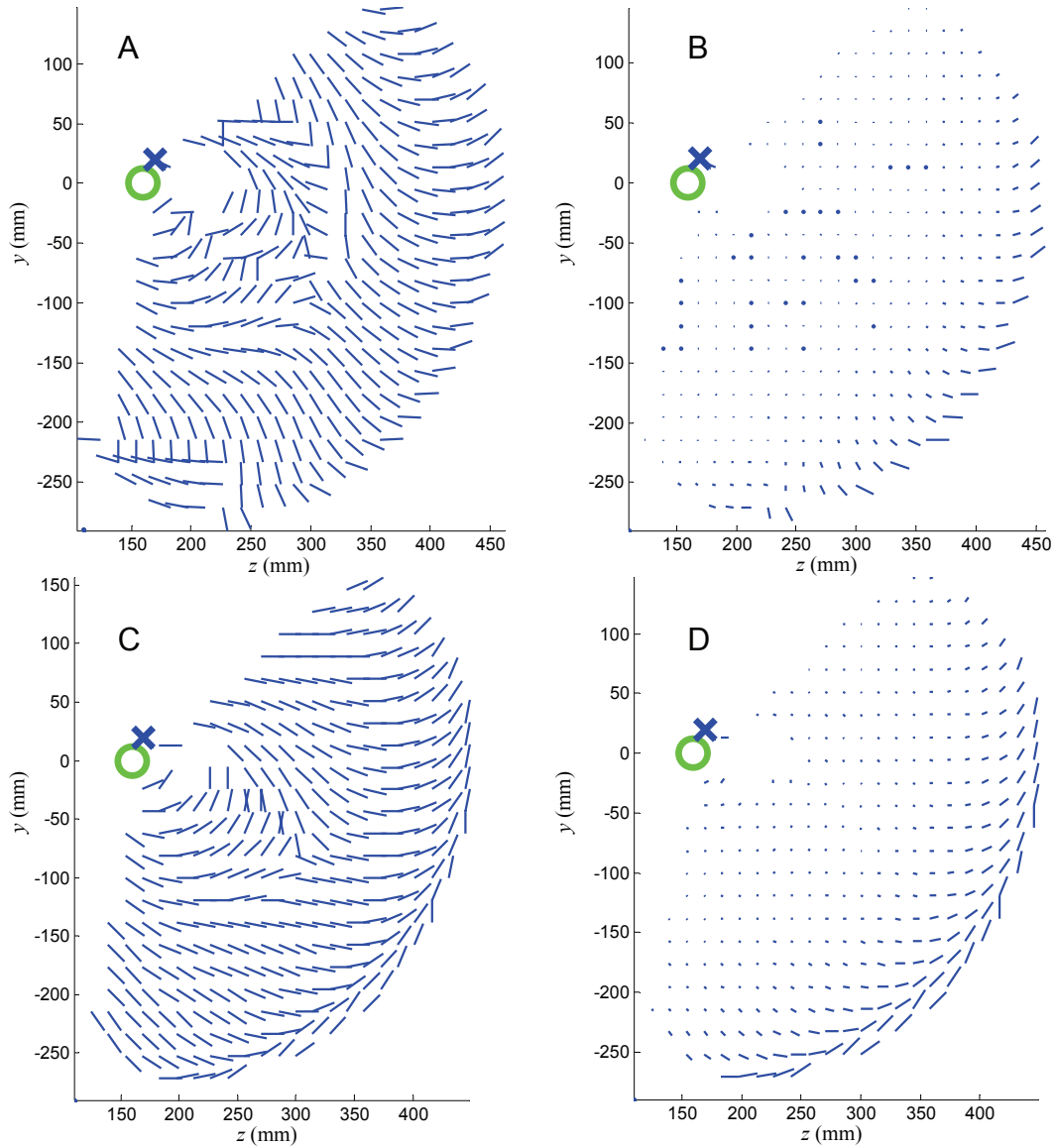


Figure 2.5. (A) Direction of desired motions that result in maximum Cartesian error length, v_σ ; (B) v_σ scaled by $\|G\|_{l_2}$; (C) Direction of desired motions that result in maximum absolute angular error, p_ϕ ; (D) p_ϕ scaled by $|\phi_{\max}|$. The circle shows the true incision location. The 'x' is the estimated incision location.

Different error directions in the port estimate were simulated (Fig. 2.6). The errors are 10 mm in the $+z$, $-z$, $+y$ and $-y$ directions, respectively. $\hat{\phi}_{\max}$ is again shown to be a conservative estimate of $|\phi_{\max}|$. Port position errors in the z -direction cause greater error at the bottom of the workspace, whereas port errors in the y -direction cause more error on the right side of the workspace. Looking more closely, positive y errors in the port position cause the high error region to shift downward compared to negative y errors in the port position. Positions along the line passing between the true and estimated port do not have motion errors.

2.3.2. Physical Experiment

The experimental setup incorporated a desktop robot (Phantom Premium 1.5, Sensable Technologies, Inc.; Woburn, MA) (Fig. 2.7). For this setup, motions were restricted to a 2D plane for easy representation of results. The controller in Fig. 2.1 was used to control the robot. The joint level controller was proportional-integral-derivative (PID) with the same 1000 Hz update rate as the inverse Jacobian control. The PID gains were chosen for a slow, over-damped motion to any position within the workspace.

A stainless steel rod 320 mm in length was attached to the end of the robot to emulate a surgical instrument. This shaft passed through a gimbal acting as a port constraint. For this work, the port constraint was placed halfway along the shaft in the z direction, at position ($y=0$ mm, $z=160$ mm). The controller used an estimated port position of (20, 170) to introduce kinematic error. Since the true port position was known, the instrument tip position (x in Fig. 2.1) was calculated using forward kinematics.

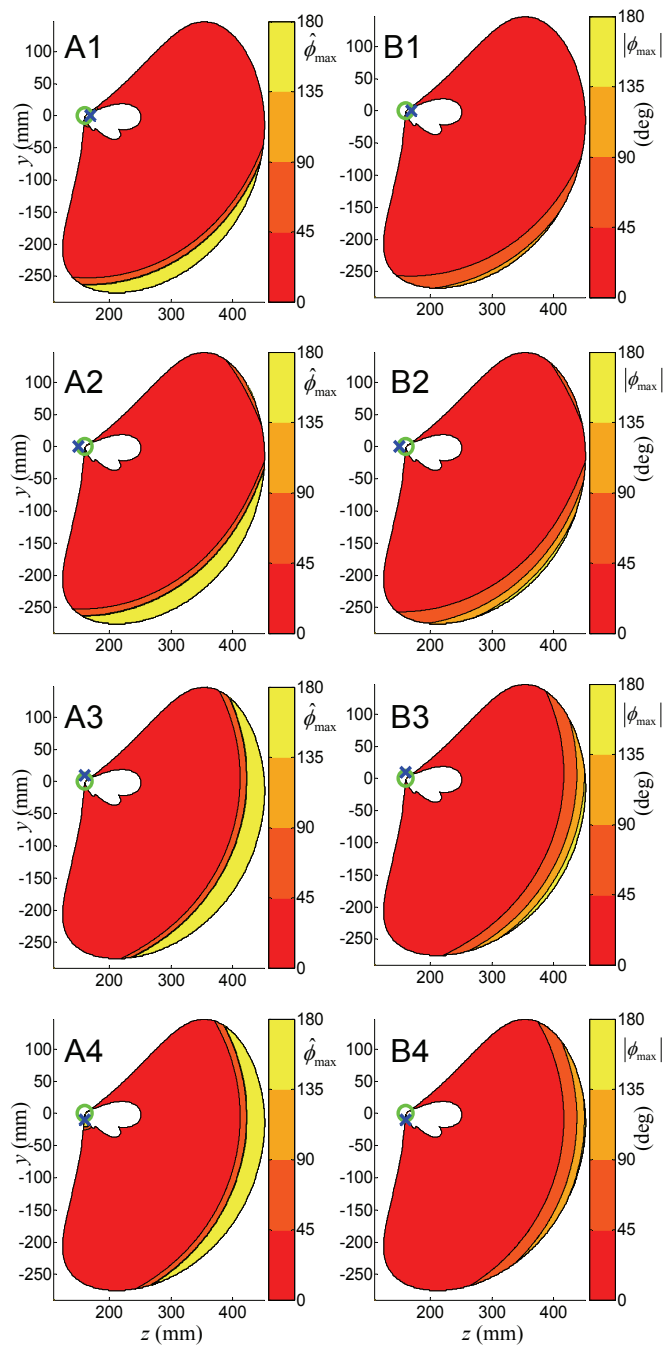


Figure 2.6. (A) $\hat{\phi}_{\max}$ (degrees). (B) $|\phi_{\max}|$ (degrees). Each with 10 mm port positioning error in a different direction: (1) $+z$. (2) $-z$. (3) $+y$. (4) $-y$. A circle shows the true incision location. An 'x' shows the estimated incision location.

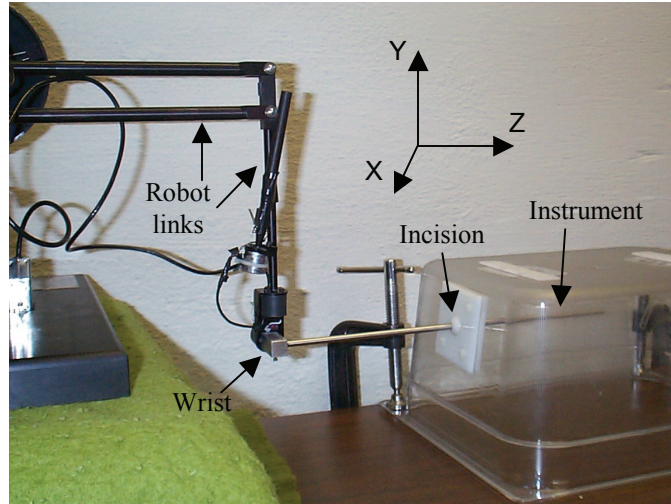


Figure 2.7. Experimental setup with axes.

For the experiment, initial tip positions were placed at (y,z) : $(0, 320)$, $(0, 375)$, and $(0, 415)$ (labeled $L-N$ in Fig. 2.4). Those positions lie in areas of increasing error. Eight desired positions were then chosen for each start position at distances of ± 20 mm along the y -axis, z -axis and diagonal directions. Experimental position data were gathered as the system moved from each start position to the corresponding eight desired positions (Fig. 2.8). Simulated paths overlay the plots in dashed lines, calculated as quasi-static steps with a controller gain of 0.01. Though none of these results show the robot moving away from the desired position before converging, such a path is possible. The simulated path for the desired position at $(435, 0)$ actually does move away from the desired position just before converging.

2.4. Discussion

A measure, $\hat{\phi}_{\max}$, was proposed for minimally invasive surgical robots with inverse Jacobian controllers. Given the true Jacobian and the estimated Jacobian, $\hat{\phi}_{\max}$ conservatively estimates the maximum absolute angle, $|\phi_{\max}|$, between desired motion and

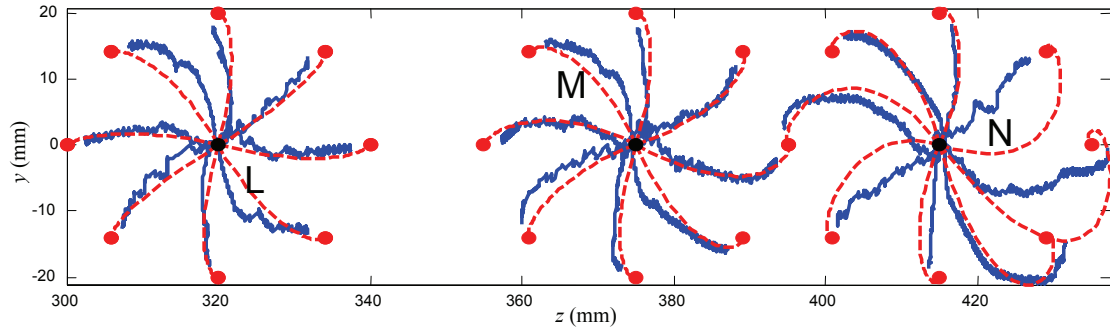


Figure 2.8. Trajectories followed in experiment (solid lines) and simulation (dashed lines), to the desired positions (red dots) each 20 mm away from the corresponding start positions (black dots) at (L): (320, 0), (M): (375, 0), (N): (415, 0).

actual motion. Possible applications in control of orientation have been left for future work. This measure assumes a quasi-static system, an assumption justified by low gain on the inverse Jacobian controller, a high-speed joint-level controller, and the presence of damping.

Simulation demonstrated the measures of the motion error across the workspace, validating $\hat{\phi}_{\max}$ as a conservative estimate of $|\phi_{\max}|$. The contours of $\hat{\phi}_{\max}$ are much steeper than those of $|\phi_{\max}|$. This results in $\hat{\phi}_{\max}$ closely estimating $|\phi_{\max}|$ around the middle of the workspace, but being quite large at positions close to, or far from, the port.

$\hat{\phi}_{\max}$ and $\|G(\theta, k)\|_{i_2}$ require knowledge of the true Jacobian of the system. When the kinematic error sources are bounded, calculating $\|G(\theta, k)\|_{i_2}$ for the worst cases shows whether the robot will converge with a monotonically decreasing error length for all possible cases. This calculation also determines the subsets of the workspace where the behavior of the system is most desirable. Similarly, the measure can be used as a design tool to determine the necessary tolerances of various system components. Using the system in this chapter as an example, if positions along $y=0$ are the most important,

then Fig. 2.6 shows that errors in the y position of the port are less tolerable than errors in the z position.

Another practical result lies in using angular errors to predict error sources. Using an external position measuring system to track the tip position, a plot of the measured errors in angle, ϕ , throughout the workspace could be composed. By comparing those measurements to the various plots of $|\phi_{\max}(\theta)|$ generated by assuming different sources of error, similarities could suggest which sources of error are significant.

The desired motions, v_σ , plotted in Fig. 2.5a, are similar to the desired motions, p_ϕ , in Fig. 2.5c. Therefore, the desired motions that result in the largest length of Cartesian error for a unit controller gain are similar to the motions that actually result in the largest angular error. The differences occur wherever changing the motion scaling gain of the inverse Jacobian controller could decrease the Cartesian error.

Path planning is another practical use for this work. If the likely sources of error are known, v_σ can easily be calculated for those error sources. A path planner could then trade off between indirect and direct paths to the desired final position, where the indirect paths may have less error than the direct paths.

Experimental results approximately followed simulation results, validating the simulation. The most obvious differences are for the start position closest to the edge of the workspace. For this start position, three of the experimental paths do not closely follow the simulated paths. Another difference between experimental and simulated paths is that the angular error between desired motion and actual motion is sometimes greater for the experimental paths than for the simulated paths. The combination of three sources of error could explain these discrepancies. First, friction at the port constraint impedes

motion anisotropically. Second, lack of gravity compensation in the joint-level control for the experimental setup results in unmodeled forces on the system that vary over the workspace. Third, dynamic effects could influence the experimental system, though this seems unlikely since the controller gains were set for slow motion.

Chapter 3

Model-Based Error Correction for Flexible Instruments

3.1. Introduction

In terms of robot control, instrument flexibility alters the kinematic structure of the manipulator so that the predicted relationship between the robot's joint and tip coordinates becomes inaccurate. A model-based controller is a logical approach to reducing flexion-induced errors. In this chapter a mechanical model of the instrument shaft deflection is developed based on a beam that is pinned at each end and is acted on by a point load. Using the developed model and tip tracking, a real-time method is proposed to reduce errors in surgical instrument control. The convergence metric introduced in the previous chapter is used to quantify the convergence of the resulting Jacobian controller in the presence of sensor error. Simulations compare the resulting controller with a controller assuming a rigid instrument shaft. Sensitivity analysis shows the effect of various levels of measurement noise on the proposed controller.

3.2. Controller Design

Fig. 3.1 diagrams a robot-assisted surgical procedure in which the instrument shaft is flexing. For the purposes of the following analysis, the instrument shaft is modeled as a

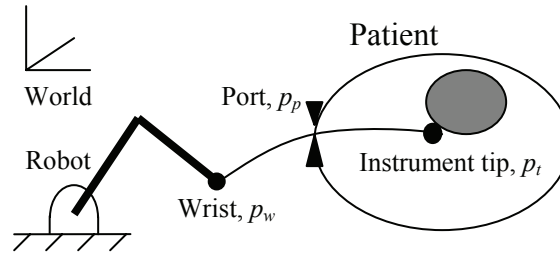


Figure 3.1. 2D Flexion in surgical instrument shaft due to force on tip.

straight rod, connected to the robot arm at a wrist. The controller's job is to accurately position the tip in a world coordinate frame. As the instrument tip interacts with tissue, radial tip forces generate reaction forces at the port and at the robot wrist. These forces result in bending of the instrument.

3.2.1. Flexion Model

The goal is to determine the actual kinematics of the instrument, i.e. its shape as it flexes during the procedure. The Euler-Bernoulli beam bending equations were chosen to model the instrument flexion, with an assumption the configuration is a pinned-pinned beam with a point load, i.e., the wrist, port, and tip apply only forces normal to the shaft and no moments (Fig. 3.2). The pinned-pinned beam with a point load fits the situation where just the tip of the instrument is in contact with the patient and precludes complicated shapes such as s-curves in the interest of low complexity. Buckling forces are small enough to be neglected in this shape computation. From [Lardner 94], the

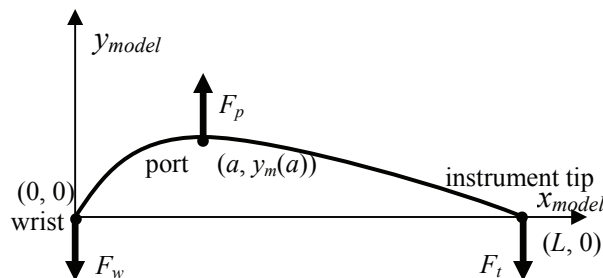


Figure 3.2. Simply supported beam model of instrument shaft in model space.

height of the beam in model coordinates is

$$y_m(x_m) = \frac{-F_p}{6EI} \left(Lbx_m \left(1 - \frac{b^2}{L^2} - \frac{x_m^2}{L^2} \right) + \langle x_m - a \rangle^3 \right) \quad (3.1)$$

and the slope of the beam is

$$y_m'(x_m) = \frac{-F_p}{6EI} \left(Lb \left(1 - \frac{b^2}{L^2} - \frac{3x_m^2}{L^2} \right) + 3\langle x_m - a \rangle^2 \right) \quad (3.2)$$

where x_m is the position along the beam, F_p is the force at the port acting at a distance a along the beam from the wrist, L is the total length of the beam, $b \equiv L - a$, E is the Young's modulus, I is the cross sectional moment of inertia, and

$$\langle x_m - a \rangle^1 = \begin{cases} 0 & x_m \leq a \\ (x_m - a) & x_m \geq a \end{cases} \quad (3.3)$$

F_p and a are the two unknowns in this model, so two measurements of the beam position, slope, or curvature are necessary for a solution. Additionally, measurements are necessary for registration between world coordinates and model coordinates.

The instrument positions and orientations (slopes) are sensed near both ends: at the tip end using either electromagnetic or visual sensing, and at the wrist end using either electromagnetic or robot arm kinematic sensors (e.g., high resolution joint encoders). These measurements permit calculation of the model parameters, and thus the Jacobian relating the motion of the beam's endpoints. Similarly, the port position or wrist force, port force, or tip force could be measured directly instead of the sensors used here; such alternatives are evaluated in the Discussion section below.

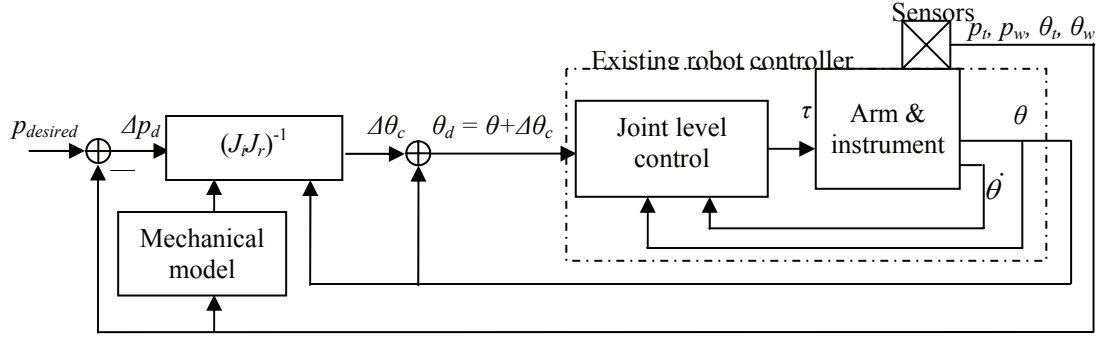


Figure 3.3. Block diagram of controller.

3.2.2. Jacobian Construction

Fig. 3.3 diagrams the inverse-Jacobian controller used in this chapter. Like in the previous chapter, the premise is that the existing joint level controller accepts a desired angular configuration

$$\theta_d = \theta + (J_i J_r)^{-1} (p_{desired} - p_t) \quad (3.4)$$

where θ is the vector of current joint angles, J_r is the robot Jacobian relating joint motions to wrist motions, J_i is the Jacobian relating motions of the wrist end of the instrument shaft to motions of the tip end, $p_{desired}$ is the desired tip position, and p_t is the current tip position. We assume that the robot arm can precisely position the wrist and the robot's Jacobian is known, so our task is to find the Jacobian for the instrument shaft. For clarity, we consider position control in 2-D here; orientation control and extension to 3-D are discussed below.

The Jacobian of the instrument shaft is constructed by taking the partial derivative of the tip position with respect to the robot wrist position

$$J_i = \begin{bmatrix} \frac{\partial x_t}{\partial x_w} & \frac{\partial x_t}{\partial y_w} \\ \frac{\partial y_t}{\partial x_w} & \frac{\partial y_t}{\partial y_w} \end{bmatrix} \quad (3.5)$$

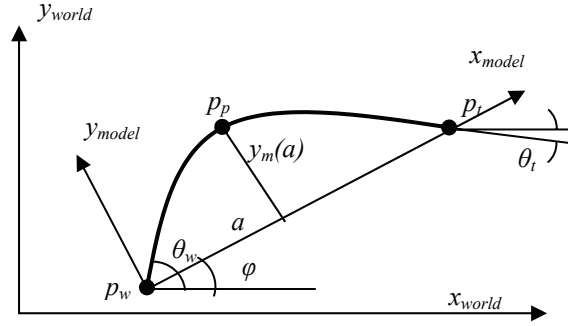


Figure 3.4. Relationship between world and model frames

where $p_w = (x_w, y_w)$ is the robot wrist position in world coordinates, and $p_t = (x_t, y_t)$ is the instrument tip position in world coordinates. The position of the instrument tip in world coordinates can be written as a transformation from model coordinates

$$\begin{bmatrix} x_t \\ y_t \end{bmatrix} = L \begin{bmatrix} \cos(\varphi) \\ \sin(\varphi) \end{bmatrix} + \begin{bmatrix} x_w \\ y_w \end{bmatrix} \quad (3.6)$$

where φ is the angle between model coordinates and world coordinates (Fig. 3.4). To incorporate the port location, p_p , which, as the instrument's fulcrum, determines the kinematic relationship between the wrist and tip, this angle can be written as

$$\varphi = \arctan\left(\frac{y_p - y_w}{x_p - x_w}\right) - \arctan\left(\frac{y_m(a)}{a}\right). \quad (3.7)$$

Combining (3.1), (3.5), (3.6), and (3.7), and performing the derivative operations in (3.5), the Jacobian can be written as a function of p_w , p_p , a , F_p , $y_m(a)$, and known parameters. Now the terms p_p , a , F_p , and $y_m(a)$ must be written as functions of the position and angle measurements at the instrument endpoints, p_w , p_t , θ_w , and θ_t . The port position in world coordinates can be written as a transformation from its position in model coordinates

$$\begin{bmatrix} x_p \\ y_p \end{bmatrix} = \begin{bmatrix} \cos(\varphi) & -\sin(\varphi) \\ \sin(\varphi) & \cos(\varphi) \end{bmatrix} \begin{bmatrix} a \\ y_m(a) \end{bmatrix} + \begin{bmatrix} x_w \\ y_w \end{bmatrix} \quad (3.8)$$

$$\varphi = \arctan\left(\frac{y_t - y_w}{x_t - x_w}\right). \quad (3.9)$$

From (3.1), the deflection height at the center force can be written in terms of F_p and a

$$y_m(a) = -\left(\frac{F_p}{EI}\right)\left(\frac{a^2(a-L)^2}{3L}\right). \quad (3.10)$$

F_p and a can be written as functions of the orientation measurements

$$F_p = \frac{2EI(y_m'(0) - y_m'(L))}{a(a-L)} \quad (3.11)$$

$$a = \frac{L(2y_m'(L) + y_m'(0))}{y_m'(L) - y_m'(0)} \quad (3.12)$$

where

$$y_m'(0) = \tan(\theta_w - \varphi) \quad (3.13)$$

$$y_m'(L) = \tan(\theta_t - \varphi). \quad (3.14)$$

Combining these equations permits calculation of the desired form of the 2D Jacobian.

$$J_i = \begin{bmatrix} J_{1,1} & J_{1,2} \\ J_{2,1} & J_{2,2} \end{bmatrix} \quad (3.15)$$

$$J_{1,1} = 1 + L \sin(\gamma - \varphi) \left(\frac{\Delta Y}{L_{meas}^2} + \frac{\Delta X (temp2 - temp1)}{temp3} \right) \quad (3.16)$$

$$J_{1,2} = L \sin(\gamma - \varphi) \left(\frac{-\Delta X}{L_{meas}^2} + \frac{\Delta Y (temp2 - temp1)}{temp3} \right) \quad (3.17)$$

$$J_{2,1} = -L \cos(\gamma - \varphi) \left(\frac{-\Delta Y}{L_{meas}^2} + \frac{\Delta X (temp1 - temp2)}{temp3} \right) \quad (3.18)$$

$$J_{2,2} = 1 - L \cos(\gamma - \varphi) \left(\frac{\Delta X}{L_{meas}^2} + \frac{\Delta Y (temp1 - temp2)}{temp3} \right) \quad (3.19)$$

$$\gamma = \arctan\left(\frac{y_m(a)}{a}\right) \quad (3.20)$$

$$temp1 = 3Ly_m(a) \quad (3.21)$$

$$temp2 = (2a - L)temp1 \quad (3.22)$$

$$temp3 = (3La + temp2 * y_m(a))(a^2 + y_m(a)^2) \quad (3.23)$$

$$\Delta X = x_p - x_w \quad (3.24)$$

$$\Delta Y = y_p - y_w \quad (3.25)$$

$$L_{meas} = (\Delta X^2 + \Delta Y^2)^{\frac{1}{2}} \quad (3.26)$$

3.3. Controller Evaluation

The convergence metric (2.6) is used to compare the proposed controller with a controller based on kinematics of a straight shaft. The metric is also used to determine the sensitivity of the proposed controller to sensor noise.

3.3.1. Comparison with a Rigid Instrument Model

The controller for the Zeus Surgical System assumes a straight instrument shaft and uses a Jacobian based on the lever equation

$$p_t = \frac{L(p_p - p_w)}{\|p_p - p_w\|} + p_w. \quad (3.27)$$

Without direct measurement, the port position, p_p , is estimated over successive controller cycles, as the intersection point of rays drawn along the instrument shaft as measured by wrist sensors. To quantify the benefits of tip tracking, the distance can be calculated between the actual tip position and the tip position estimated by the lever equation. To

calculate the actual tip position, first the right triangle formed by a and $y_m(a)$ is solved for a (Fig. 3.4)

$$\|p_p - p_w\|^2 = a^2 + y_m^2(a) \quad (3.28)$$

with (3.1) substituted in for $y_m(a)$. Then (3.1), (3.6), and (3.7) are combined to calculate the tip position. In addition, to quantify the benefits of the flexion model, the convergence metric can be used to compare the lever Jacobian with the flexion Jacobian. The rigid instrument Jacobian is calculated by substituting (3.27) into (3.5).

3.3.2. Sensitivity Analysis for Jacobian

To compute the effects of sensor noise on the proposed controller, the convergence metric is used again. The flexion model Jacobian is substituted into (3.15) as both the true and estimated Jacobians, the latter instance being calculated with additive sensor noise. The noise has a uniform distribution along each sensor axis, with maximums listed in the figures (up to $0.002L$ in position and 0.002 rad in angle) and minimums equal to the negatives of the maximums. The convergence metric is then evaluated at various insertion depths and with various magnitudes of sensor noise. For a given insertion depth, the maximum error across noise values is determined. One of the advantages of the flexion model is an estimate of the port position, the accuracy for which is unaffected by flexion. Error in port localization due to sensor noise is also calculated.

3.4. Results

For all plots, the tip and wrist forces will be assumed to act such that F_w and F_t are in the $-y_m$ direction in model coordinates; axial forces in the x_m direction do not produce

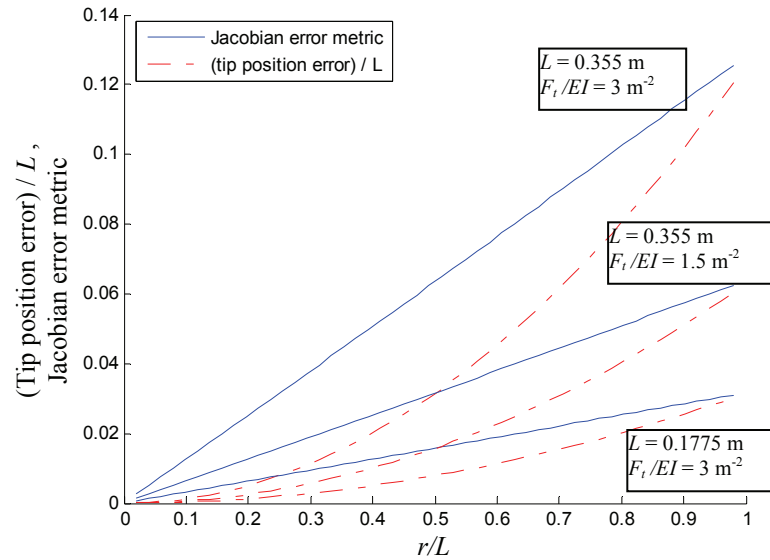


Figure 3.5. Position error and Jacobian motion increase as the instrument tip is inserted farther into the port.

bending. Taking advantage of rotational symmetry about the port, all plots show the values as a function of insertion depth, $r = [(x_t - x_p)^2 + (y_t - y_p)^2]^{1/2}$.

3.4.1. Comparison with a Rigid Instrument Model

The greater the insertion depth, the larger the error in tip position calculated from the forward kinematics of a straight shaft (Fig. 3.5). Additionally, the motion error for the straight shaft based Jacobian is proportional to the insertion depth, as determined by (3.16) with the flexion model Jacobian as the true Jacobian.

3.4.2. Sensitivity Analysis for Jacobian

Noise in the position and orientation measurements degrades the performance of the flexion model Jacobian. To demonstrate these effects, (3.16) was calculated across the tip workspace, using the flexion Jacobian with noise in each measurement for the estimated Jacobian and without measurement noise for the true Jacobian. The following plots show the worst (maximum) values across all noise directions.

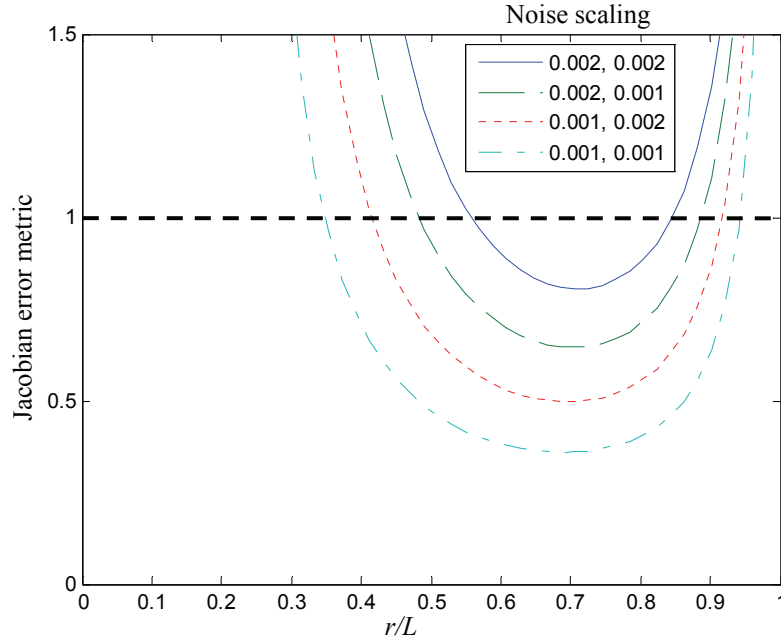


Fig. 3.6. The motions commanded by the flexion based Jacobian become less accurate as sensor noise increases. Values greater than 1 signify divergent motions. The first scaling number is the position error scaling, with respect to L . The second number is the angular error (rad). $L = 0.355$ m. $F_t/EI = 3$ m⁻².

In the presence of sensor noise, the motion errors from the flexion model Jacobian are smallest when the instrument is inserted approximately 70% of its length (Fig. 3.6). The motions become divergent as either the tip or the wrist move close to the port. Decreasing the sensor noise reduces the controller's motion errors.

The estimated parameters, F_p and a , can also be examined. Since F_p and the structural rigidity, EI , always enter the beam bending equations together, the term F_p/EI was estimated. This term can be thought of as a normalized force. F_p/EI can be incorrect by orders of magnitude outside of the convergent area due to the measurement noise, but improves as r/L approaches 0.5 (Fig. 3.7). The error in estimating the port position decreases as the instrument tip moves further from the port (Fig. 3.8). Increasing the instrument length, L , or the normalized force, F_t/EI , increases the convergence of the controller, similar to decreasing sensor noise (Fig. 3.9). Increasing these parameters

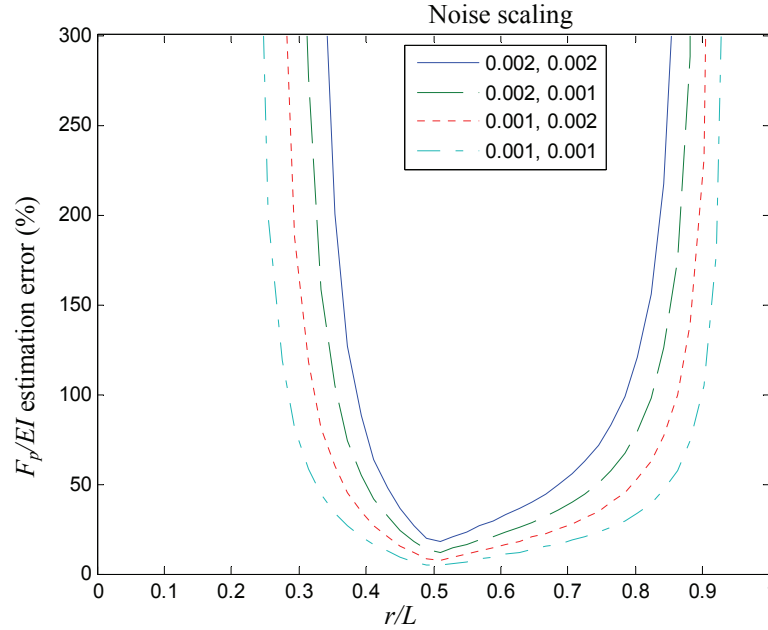


Fig. 3.7. In the presence of sensor noise, F_p/EI is best estimated in the center of the workspace. The first scaling number is the position error scaling, with respect to L . The second number is the angular error (rad). $L = 0.355$ m. $F_t/EI = 3$ m².

increases flexion for a constant tip force. For a given level of sensor noise, increasing the flexion would increase the signal-to-noise ratio, explaining the similarity between Figs. 3.6 and 3.9.

3.5. Discussion

Tracking the instrument tip in minimally invasive surgery avoids errors in the forward kinematics and allows a more accurate kinematic model for motion control. The model-based controller presented here for flexible instrument shafts can reduce motion error in comparison with controllers assuming rigid links. Barring sensor noise, the flexion model commands accurate motions for a flexed instrument whereas the straight shaft model results in motion errors.

To compare the sensor noise magnitudes used in this paper to a commercial product, the measurement noise of an electromagnetic tracking system was determined (Minibird,

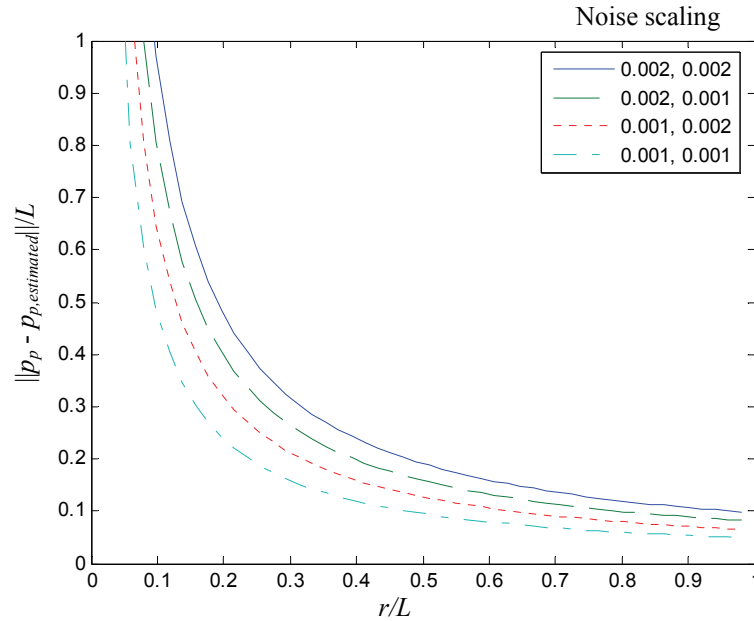


Figure 3.8. The error in port position estimation decreases as insertion depth increases. The first scaling number is the position error scaling, with respect to L . The second number is the angular error (rad). $L = 0.355$ m. $F_t/EI = 3$ m⁻².

800 Model, Ascension Technologies; Burlington, VT). Since the sensor's relative accuracy is not published, a measurement was made by fixing the sensor in place for five minutes. The measured RMS positional deviation was 0.13 mm, and the RMS angular deviation was 0.00056 rad. For this magnitude of noise with $L = 0.355$ m and $F_t/EI = 3$ m⁻², the flexion model Jacobian has smaller errors than the straight shaft Jacobian for insertion depths greater than $0.05L$. With the instrument inserted halfway through the port, the convergence metric (2.6) is 0.006 for the flexion model Jacobian. As flexion increases, the straight shaft Jacobian performs worse and the flexion model Jacobian performs better.

As shown in Fig. 3.5, the error in tip position estimation can be on the order of centimeters if a bent instrument shaft is assumed to be straight. Such an error magnitude is larger than the sizes of many surgical targets. Tip tracking measures the actual position

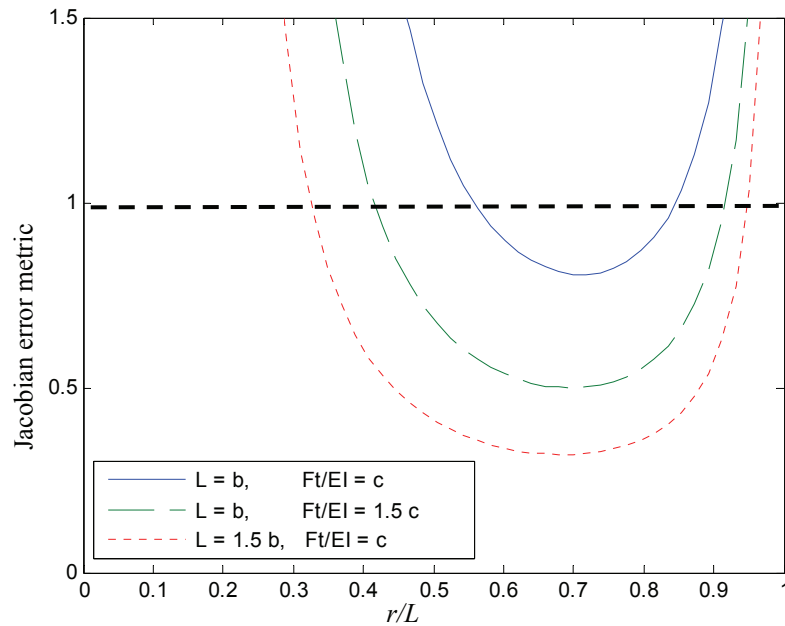


Figure 3.9. The motions commanded by the flexion based Jacobian become more accurate as either L increases or the tip force increases. $b = 0.355$ m. $c = 3$ m⁻². The noise magnitude is $0.002L$ for the position measurements and 0.002 rad for the angle measurements. Values greater than 1 signify divergent motions.

of the tip, allowing effective image guidance. The benefit of tip tracking for robotic surgery is explored in greater detail in Chapter 5.

In this chapter, the orientations of the instrument's endpoints are used to solve for the flexion model parameters. Alternative possibilities include measuring the port position and orientation, and forces/torques on the wrist, port, and tip. In Chapter 4, strain gages are bonded to an instrument and the measured strains are used to calculate the model parameters. The downside to strain gages is the prohibitive cost, since MIS instruments are disposable. Attaching a force/torque sensor to the instrument at the robot's wrist is feasible, but only provides one independent measurement. Measuring the force or torque at the port would require a custom built port. Accurately measuring the position and orientation of the instrument shaft at the port is difficult due to the uncertain relationship between the physical port and any contact points between the port and the instrument

shaft. For these reasons, electromagnetic sensors attached to the instrument are the most practical method of fitting the model and determining the tip position.

The flexion model Jacobian in this chapter only handles motions in the plane containing the instrument, but is extended to 3-D in Chapter 5. If the robot exerts a force on the instrument that is perpendicular to the plane of bending, torque will be generated at the port position. The entire plane of bending will then rotate about a line that passes through the port position.

Orientation control can be achieved by calculating the Jacobian relating the change of orientation of the tip to the change in position of the wrist. Assuming infinitesimal motions, moving the wrist does not change the shape of the beam, so the only change in orientation is caused by the changing registration between the model and world coordinates. The columns of the positional Jacobian matrix describe the tip motions resulting from wrist motions along the world axes, allowing calculation of the consequential change in rotation.

In the interests of a better fit between the model and the true instrument shaft shape, the simply supported configuration can be replaced with a more complicated assumption of the shape. The new configuration would allow the controller to handle more complex instrument/environment interactions, but would contain more unknowns and thus require correspondingly more measurements. Those measurements could come from a force/torque sensor as discussed above or from additional position and orientation measurements.

Chapter 4

Experimental Validation in Two Dimensions

4.1. Introduction

The previous chapter presented a model based controller for improving surgical instrument tip motions in the presence of a flexing instrument shaft and a moving endoscopic port. By applying the metric from Chapter 2, the convergence properties of the controller were shown to be sensitive to noise in the sensor measurements used to fit the model. This chapter experimentally evaluates the performance of the controller for a flexed instrument shaft, compared with a controller assuming the instrument shaft is straight. In the first experiment, the flexion is introduced through a mass hung from the instrument tip. In the second experiment, the flexion is caused by indenting an elastic surface with the instrument tip. To demonstrate that the system is not dependant on specific sensors, two separate sensor modalities are used to fit the model, electromagnetic position/orientation sensors and strain gages.

4.2. Calculating Model Parameters

This work uses the model presented in Fig. 3.2 with the controller from Fig. 3.3. To demonstrate that the model can be used with various sensor modalities, two methods are

used to determine the model parameters. The first method uses measurements of the wrist, port, and tip orientations in a real-time nonlinear search to estimate the model parameters from (3.2). Three measurements are used to fit two parameters in order to reduce the system's sensitivity to noise in the orientation measurements. The second method of solving for the model parameters uses moments at two positions on the instrument, one on either side of the port. From [Lardner 94], the moment at a given position on the beam is

$$M(x_m) = \frac{F_p(L-a)x_m}{L} - F_p \langle x_m - a \rangle. \quad (4)$$

The model parameters are therefore

$$a = \frac{M(x_{tip\ moment})x_{wrist\ moment}L}{M(x_{tip\ moment})x_{wrist\ moment} + M(x_{wrist\ moment})(L - x_{tip\ moment})} \quad (5)$$

$$F_p = \frac{M(x_{wrist\ moment})L}{x_{wrist\ moment}(L - a)} \quad (6)$$

where $x_{wrist\ moment}$ is the x -position in model coordinates of the moment measurement near the wrist, and $x_{tip\ moment}$ is the x -position in model coordinates of the moment measurement near the tip. For both methods of determining the model parameters, position measurements at the wrist and tip are used to register model coordinates with world coordinates. The Jacobian is then constructed as outlined in the previous chapter. Other sensor modalities can be used to derive these measurements, as covered in the discussion for Chapter 3.

4.3. Methods

The setup in Fig. 4.1 was used to evaluate the proposed flexion controller. A desktop robot (Phantom Premium 1.5, Sensable Technologies, Inc.; Woburn, Mass.) held onto a stainless steel shaft 600 mm long, 2.38 mm diameter. The shaft passed through a port consisting of a 2.49 mm diameter hole drilled through a 26 mm long Teflon block. The block was supported by a frame allowing free rotation in response to robot motions. Electromagnetic sensors (Minibird model 800, Ascension Technology, Inc.; Milton, VT) were attached to the system at three locations: the Teflon block, the robot's wrist, and 40 mm from the tip of the shaft. The position and orientation of each sensor was measured at 120 Hz. The position measurement of the port sensor was not used in these experiments. In addition, four silicon strain gages were bonded to the shaft, two 150 mm from the wrist and two 100 mm from the tip. One gage from each pair was attached to the top of the shaft, the other to the bottom. The strain measurements were used to calculate the moments at both locations.

The proposed controller was commanded to drive the shaft tip along various trajectories while tip position measurements were recorded. Then the model based Jacobian was replaced with a Jacobian calculated from the kinematics of a straight shaft, as described in the previous chapter, and that system was commanded to follow the desired trajectories. First, trials with a constant tip force were simulated and performed

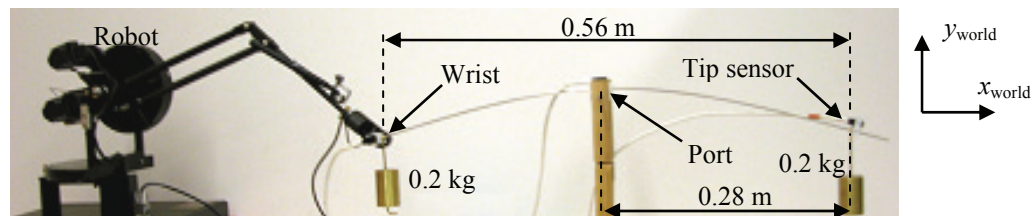


Fig. 4.1. Experimental setup.

experimentally. Then, experimental trials were performed with a position-dependent tip force that more closely simulates the surgical environment.

4.3.1. *Simulation*

A quasi-static simulation predicted controller behavior. For the simulation, the tip force was 2 N, and the initial wrist position was set to 280 mm in the $-x$ direction from the port position. A nonlinear search determined the port force, F_p , and the x -position of the port in model coordinates, a , that would satisfy the force balance and the distance between wrist and port. Once F_p and a were known, (3.1) was used to calculate the position of the port in model coordinates. The port and wrist positions were then used to register model coordinates with world coordinates and (3.6) calculated the tip position. The wrist and tip orientations were calculated from (3.2).

To simulate the sensor measurements, the positions and orientations were summed with additive noise. The noise had a uniform distribution with a maximum magnitude in each axis of 1.8 mm for positions and 0.0087 rad for angles. These noise magnitudes were chosen to match the published specifications for the RMS accuracy across the workspace of the electromagnetic sensors used in the experiments.

The controllers were given the simulated sensor values and the desired tip trajectory. Four trajectories were used, one in each of $+x$, $-x$, $+y$, and $-y$ directions. The trajectories were 10 mm long and had four intermediate points spaced 2 mm apart. This spacing was chosen for ease of viewing the results. Varying the spacing affects both controllers equally, leaving the relative results unaffected. The first controller update was calculated for a 2 mm motion. The desired position for the second controller update was 4 mm from the initial position. For any update after the fourth, the desired position was 10 mm from

the initial position. After the controller calculated the wrist motion and therefore the new wrist position, the model calculations were performed again to determine the new tip position. The cycle continued until the tip reached the desired position.

4.3.2. Experiments

The first set of experimental trials were quasi-static for comparison with the simulation. The effects of dynamics were removed by running the joint level feedback loop until the tip settled to some position. Then the outer loop of the controller was run once, calculating new desired joint angles via (3.4). These steps repeated until the tip reached the final desired position. The desired trajectories, port position, and initial robot position were the same as for the simulation. A 0.2 kg mass was hung on the shaft next to the tip sensor to enforce shaft flexion. An identical mass was hung next to the robot's wrist as a counterbalance.

For the dynamic trials, flexion was caused by indenting the shaft's tip into a block of silicone (50 mm x 86 mm x 86 mm, elastic modulus 10.8 kPa) while the outer control loop updated at 120 Hz and the joint level control updated at 2000 Hz. The joint level control was a proportional-integral-derivative (PID) feedback loop with the same gains for all trials. In these trials, the tip initially rested on the edge of the top of the silicone block. The controller was given a desired position 15 mm down into the silicone. Once the tip reached the desired position, the controller was commanded to return to the original position on the surface of the block. These trials were completed five times each for the controller using the straight shaft kinematics, the proposed controller using orientation measurements, and the proposed controller using strain measurements. The silicone was dusted in talcum powder to reduce friction and sticking.

4.4. Results

Results from simulation (Fig 4.2), quasi-static experiments (Fig. 4.3), and dynamic experiments (Fig. 4.4) show that the proposed controller is more accurate than the straight shaft controller. Across all simulations, the flexion controller resulted in a maximum deviation from the desired path of 0.8 mm compared to 1.8 mm for the straight shaft controller. In the quasi-static experiments, the maximum deviation for the flexion controller was 1.1 mm, compared with 1.9 mm for the straight shaft controller. Across all dynamic trials, the flexion controller's maximum deviation from the desired path was 1.1 mm when using orientation measurements to fit the model parameters, compared with 0.94 mm using strain measurements, and 2.6 mm for the straight shaft controller. The average over all dynamic trials of the root mean squared deviation for the flexion controller was 0.32 mm when using orientation measurements, compared with 0.35 mm for strain measurements, and 0.76 mm for the straight shaft controller. On average, each

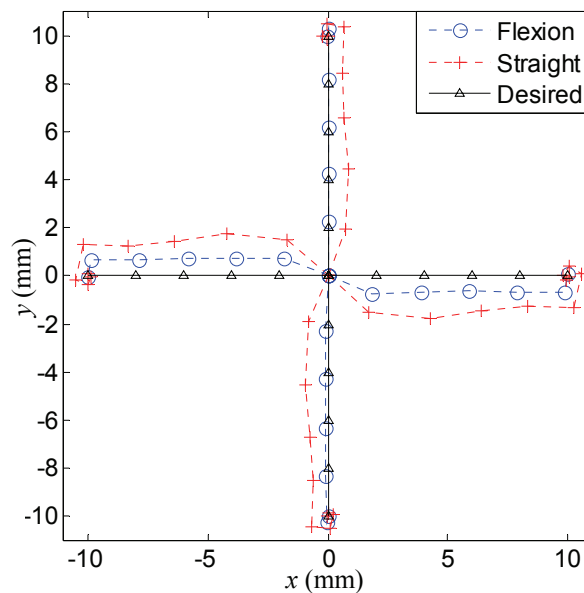


Fig. 4.2. The flexion controller causes less deviation than the straight shaft controller in simulation. A 2 N force pushed in the $-y$ direction on the tip. The port was at $(-270, 110)$.

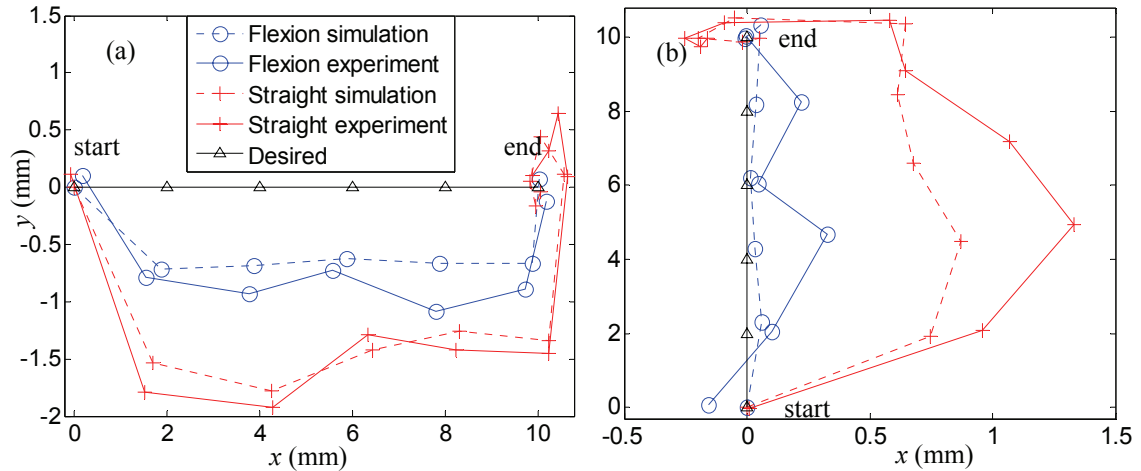


Fig. 4.3. Quasi-static experimental results confirm simulation results. Two directions of desired motions are shown, away from port (a), and up (b). There was a 2 N force in the $-y$ direction on the tip. The port was at $(-270, 110)$. Note the axes use different scales to clearly show errors.

dynamic trial took 2 seconds due to the slow response of the joint level control.

4.5. Discussion

The proposed model based controller reduces maximum path deviation caused by shaft flexion by 55% in dynamic experiments, quasi-static experiments, and quasi-static simulation, compared with a controller that assumes a straight instrument shaft. Similar results are obtained when fitting the model parameters using orientation measurements or strain measurements. Such more accurate motions increase the safety of robotic surgery and allow more precise image-guidance techniques.

4.5.1. Quasi-Static Response

In the quasi-static results, the straight shaft controller commands motions that overshoot the desired position and then spiral in. This path demonstrates how tip tracking with a Jacobian controller can converge to the desired position even in the presence of kinematic errors. This result also demonstrates that convergence is not a sufficient measure for surgical robot performance because convergent trajectories can exhibit undesirable path deviations.

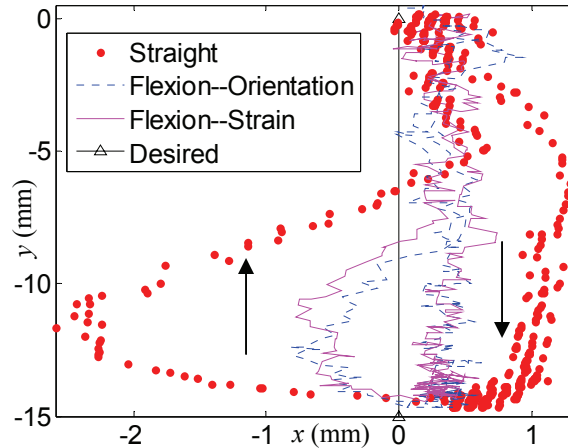


Fig. 4.4. Experimental results for indenting tip into a silicone block. Five indentations were run for each controller. Displayed trials have the median mean squared distance from the desired path. The block's upper surface is at $y = 0$. The port is at $(-300, -15)$. Arrows show direction of motion.

The flexion controller does not perfectly follow the desired trajectory because with each motion the shaft's shape changes as a function of insertion depth. Desired motions parallel to the y -axis lead to smaller deviations (maximums of 0.1 mm for the flexion controller and 0.9 mm for the straight shaft controller) than perpendicular motions due to less variation in insertion depth and correspondingly less change in shaft shape. Predicting the shaft shape after the impending motion could reduce this error, but the accuracy of such predictions would be dependent on a model of the tissue mechanics and boundaries.

4.5.2. *Dynamic Response*

In the dynamic trials, the largest deviation from the desired path occurs at the start of the upward motion. This effect is a combination of two factors, the magnitude of the flexion and the desired motion length. The further the tip presses into the silicone, the larger the tip force and corresponding flexion. As the flexion increases, the error in the straight shaft controller increases. For Jacobian based controllers with given kinematic errors, larger desired motions result in larger deviations. Thus, the deviations for the

straight shaft controller are largest at the start of the upward motion, when both the flexion and the desired motion length are at their maximums for the trial. Similarly, the flexion controller's largest deviations occur at the start of the upward motion, when the desired motion lengths are at their maximums and the shaft flexion is changing the most between controller updates. Future investigations will include a teleoperation task with desired trajectories commanded by subjects in a user study.

The average dynamic trial time of 2 seconds is a result of the joint level controller's PID gains. The combination of the robot's low transmission ratio and the environmental force prevents the proportional gain from reducing the position error to zero during the downward motion. The remaining error is reduced through the slow increase of the integral term. Increasing the proportional gain shrinks that remaining error but causes the tip to overshoot on the upstroke when the environmental force pushes towards the desired position. Sufficiently increasing the derivative gain removes that overshoot but leads to high velocity oscillations in the wrist's position. The oscillations are a result of noise in the velocity measurements and can be reduced through filtering the velocity at the cost of delay in the velocity term. The PID gains were empirically chosen for small delay in the velocity term while keeping the upstroke overshoot low and the trial duration short. Commercial surgical robots with a higher transmission ratio would not experience these considerations.

The controller responses were similar when the model parameters were fit using orientation measurements compared with strain measurements. Most likely the limiting factor in improving the proposed controller's response is the controller's update rate, which was limited by the maximum update rate for the electromagnetic sensors. With

faster position sensors to register model coordinates with world coordinates, and by using the strain measurements to fit the model parameters, the proposed controller's results would be expected to improve.

Chapter 5

3D Image-Guided Teleoperation User Study

5.1. Introduction

In the interests of developing an image-guided system that is accurate in the presence of quasi-static instrument flexion, Chapter 3 presented a controller based on a model of a flexing instrument shaft and measurements of the instrument's tip position. Chapter 4 then investigated the controller's behavior for simple two-dimensional motions. This chapter uses a three-dimensional image-guidance experiment to investigate the separate benefits of more accurate kinematics and of directly measuring the instrument's tip position. To that end, ten subjects participated in a teleoperation task using multiple controllers. The task involved instrument flexion due to interaction with a silicone tissue model. The experimental results evaluate the controllers' image-guided performances by measuring incursions into a forbidden region virtual fixture. The findings are applicable to any system where positioning accuracy is important in the presence of quasi-static flexion.

5.2. Methods

This chapter investigates the positioning accuracies of four controllers in the presence of this quasi-static instrument flexion. Two controllers use a more accurate kinematic model of the flexing instrument, and two use tip position measurements.

5.2.1. Controller Design

Fig. 5.1 diagrams the instrument control used in this chapter. The premise is that the existing joint level controller accepts a desired wrist position and that the robot arm can precisely position the wrist. The desired wrist position, $p_{w,desired}$, is calculated as a motion from $p_w = (x_w, y_w, z_w)$, the current wrist position, based on the intended change in the instrument tip position, Δp_t . $p_{w,desired}$ can be expressed as

$$p_{w,desired} = p_w + \Delta p_w = p_w + J_i^{-1} \Delta p_t \quad (5.1)$$

$$\Delta p_t = p_{t,desired} - p_t \quad (5.2)$$

where $p_{t,desired}$ is the desired tip position in world coordinates, $p_t = (x_t, y_t, z_t)$ is the current tip position in world coordinates, Δp_w is the desired wrist motion, and J_i is the instrument Jacobian relating motions of the robot's wrist to motions of the instrument tip,

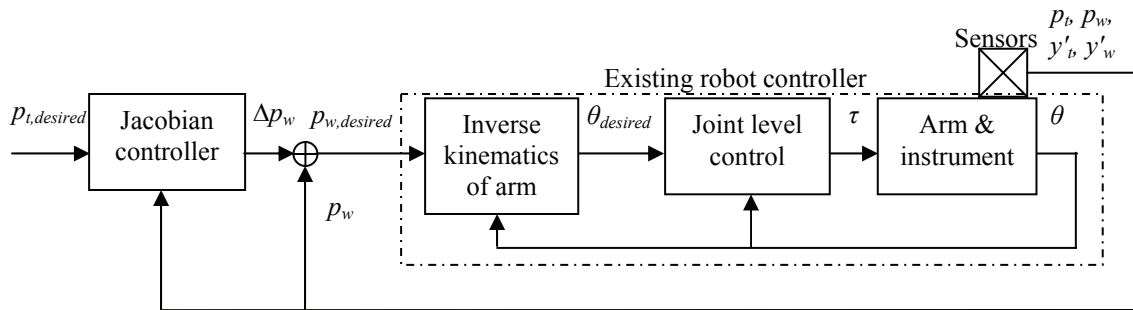


Figure 5.1. Inner and outer feedback loops.

$$J_i = \begin{bmatrix} \frac{\partial x_t}{\partial x_w} & \frac{\partial x_t}{\partial y_w} & \frac{\partial x_t}{\partial z_w} \\ \frac{\partial y_t}{\partial x_w} & \frac{\partial y_t}{\partial y_w} & \frac{\partial y_t}{\partial z_w} \\ \frac{\partial z_t}{\partial x_w} & \frac{\partial z_t}{\partial y_w} & \frac{\partial z_t}{\partial z_w} \end{bmatrix}. \quad (5.3)$$

5.2.2. Four Jacobian-based Controllers

Four Jacobian-based controllers were constructed to investigate the benefits of two separate effects, tip tracking and more accurate kinematics (Fig. 5.2). The first controller, Straight-Calculate, did not use position or orientation measurements. This controller used the kinematics of a straight rod (3.17) to calculate both the Jacobian and the desired tip motion. The Jacobian is calculated as in Chapter 3. The desired tip motion is calculated by substituting (3.17) for the tip position, p_t , in (5.2), where the port position in world coordinates, p_p , is assumed known and constant. The port position can be measured directly or inferred from instrument motions. The second controller, Straight-Track, used

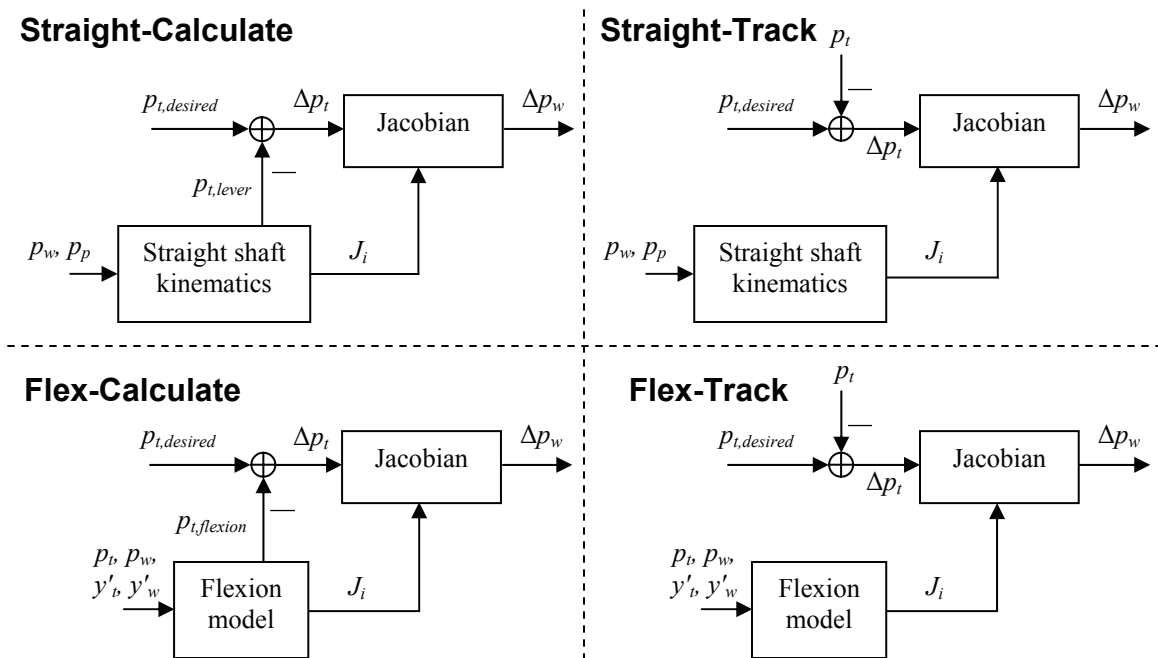


Figure 5.2. Four Jacobian-based calculations of desired wrist motion.

the same Jacobian but used position measurements of the instrument's tip to determine the tip position error. The third controller, Flex-Calculate, used the flexion model from Chapter 3 to calculate both the Jacobian and the tip position, and the fourth controller, Flex-Track, used the flexion model based Jacobian with the tip error determined from tip position measurements.

5.2.3. Flexion Model in 3D

The first task is to fit the 2D flexion model's (Fig 3.2) parameters, port force and port position, using orientation measurements at the ends of the instrument. First, the orientations in world coordinates are transformed to model coordinates. The wrist is at the origin of the model coordinates and the tip lies at a distance L along the model's x -axis, \hat{x}_m , so \hat{x}_m rotated into world coordinates is

$$\hat{v}_x = R_m^{world} \hat{x}_m = \frac{P_t - P_w}{\|P_t - P_w\|} \quad (5.4)$$

where R_m^{world} is the rotation matrix from model coordinates to world coordinates. Similarly, \hat{z}_m is the model's axis normal to the plane of curvature and \hat{v}_z is that axis rotated into world coordinates. Assuming that when the instrument is straight the sensor's x -axis points along the instrument from wrist to tip, \hat{v}_z is calculated from \hat{v}_x and k_w , the vector for the sensor's x -axis in world coordinates,

$$\hat{v}_z = R_m^{world} \hat{z}_m = \hat{v}_x \times k_w. \quad (5.5)$$

k_w is calculated from R_w^{world} , the rotation matrix for the orientation of the wrist sensor in world coordinates,

$$k_w = R_w^{world} \begin{bmatrix} 1 \\ 0 \\ 0 \end{bmatrix}. \quad (5.6)$$

The final model axis, \hat{y}_m , rotated into world coordinates is then

$$\hat{v}_y = R_m^{world} \hat{y}_m = (\hat{v}_x \times k_w) \times \hat{v}_x. \quad (5.7)$$

Thus \hat{v}_y is a vector in world coordinates that is parallel to the forces at the wrist, tip, and port.

The slopes at the ends of the instrument are calculated by projecting the orientations into the plane

$$y'_w = y'_{m,measured}(0) = \frac{(R_m^{world} \hat{y}_m) \bullet k_w}{(R_m^{world} \hat{x}_m) \bullet k_w} \quad (5.8)$$

$$y'_t = y'_{m,measured}(L) = \frac{(R_m^{world} \hat{y}_m) \bullet k_t}{(R_m^{world} \hat{x}_m) \bullet k_t} \quad (5.9)$$

$$k_t = R_t^{world} \begin{bmatrix} 1 \\ 0 \\ 0 \end{bmatrix}. \quad (5.10)$$

where R_t^{world} is the rotation matrix for the orientation of the tip sensor in world coordinates. From the slopes at the endpoints, the model parameters are

$$F_p = \frac{2EI(y'_{m,measured}(0) - y'_{m,measured}(L))}{a(a-L)} \quad (5.11)$$

$$a = \frac{L(2y'_{m,measured}(L) + y'_{m,measured}(0))}{y'_{m,measured}(L) - y'_{m,measured}(0)}. \quad (5.12)$$

5.2.4. Tip Position From Model

To calculate the tip position in world coordinates from the flexion model, as required by the Flex-Calculate controller, the tip position is transformed from model coordinates

$$P_{t,flexion} = x_{t,m}v_x + y_{t,m}v_y + P_w \quad (5.13)$$

where $x_{t,m}$ and $y_{t,m}$ are the x - and y - model coordinates for the tip. Thus the vector from the wrist position to the calculated tip position is oriented using the measured tip position, but as a result of the flexion model's "small angle" assumption, the vector length is constant and equal to the length of the straight shaft. This assumption introduces errors into the calculated tip position because the actual distance between the instrument's endpoints varies as a function of the flexion. To improve the calculated tip position, the vector length was adjusted according to large deflection equations [Belendez 02].

For this adjustment, the rod was modeled as two cantilever beams extending from either side of the port (Fig. 5.3). From the model parameters, the forces at the ends of those cantilevers are

$$F_w = \frac{F_p(L-a)}{L} \quad (5.14)$$

$$F_t = \frac{F_p a}{L}. \quad (5.15)$$

The nondimensional load parameters for each side were

$$\alpha_w = \frac{F_w a^2}{2EI} \quad (5.16)$$

$$\alpha_t = \frac{F_t(L-a)^2}{2EI} \quad (5.17)$$

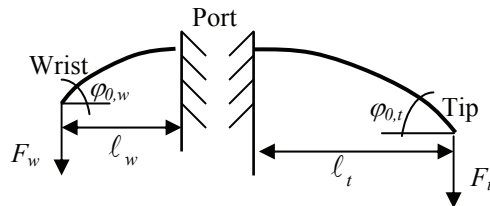


Figure 5.3. Diagram of cantilever model for calculation of wrist to tip distance of flexed beam.

and were used in a pre-calculated look-up table to determine the angles at both ends of the cantilevers, $\varphi_{0,w}(\alpha_w)$ and $\varphi_{0,t}(\alpha_t)$. The look-up table was constructed by solving

$$\alpha = \int_0^{\varphi_0} \frac{d\varphi}{4(\sin \varphi_0 - \sin \varphi)} \quad (5.18)$$

for values of φ_0 between 0 and 0.5 rad. The adjusted distance from wrist to tip is then

$$L_{cantilever} = \ell_w + \ell_t \quad (5.19)$$

$$\ell_w = \sqrt{\sin(\varphi_{0,w})} \sqrt{\frac{2EI}{F_w}} \quad (5.20)$$

$$\ell_t = \sqrt{\sin(\varphi_{0,t})} \sqrt{\frac{2EI}{F_t}}. \quad (5.21)$$

Since the ℓ_w and ℓ_t measurements are parallel with the instrument slope at the port, $L_{cantilever}$ accurately estimates the wrist to tip distance only when the instrument is inserted approximately halfway through the port. In this situation, the same curvature is experienced by both ends of the instrument and the instrument's endpoints are displaced the same distance perpendicular to ℓ_w and ℓ_t .

The x -position of the rod's tip in flexion model coordinates is then

$$\begin{bmatrix} x_{t,m} \\ y_{t,m} \end{bmatrix} = L_{cantilever} \begin{bmatrix} \cos(\gamma) \\ \sin(\gamma) \end{bmatrix} \quad (5.22)$$

where the angle of rotation is determined from (3.2) and (5.8),

$$\gamma = \arctan(y'_{m,measured}(0)) - \arctan(y'_m(0)). \quad (5.23)$$

The adjusted tip position is calculated by substituting (5.22) into (5.13).

5.2.5. 3D Flexion Jacobian

Once the model parameters, F_p and a , have been estimated, the Jacobian relating the motions of the flexed instrument's endpoints can be calculated. To calculate the Jacobian that relates 3D motions of the wrist and tip, first a Jacobian that relates the 2D motions within the plane containing the instrument is calculated in a manner similar to section 3.2.2. The tip position within the plane can be written as

$$\begin{bmatrix} x_{t,m} \\ y_{t,m} \end{bmatrix} = L \begin{bmatrix} \cos(\varphi) \\ \sin(\varphi) \end{bmatrix} + \begin{bmatrix} x_{w,m} \\ y_{w,m} \end{bmatrix} \quad (5.24)$$

$$\varphi = \arctan\left(\frac{y_{p,m} - y_{w,m}}{x_{p,m} - x_{w,m}}\right) - \arctan\left(\frac{y_m(a)}{a}\right) \quad (5.25)$$

where $p_{w,m}=(x_{w,m}, y_{w,m})$ is the x -position of the wrist in flexion model coordinates, and φ incorporates the port location, $p_{p,m} = (x_{p,w}, y_{p,m})$, which is the instrument's fulcrum and is assumed fixed in position. Taking the partial derivatives according to

$$J_{2D} = \begin{bmatrix} \frac{\partial x_{t,m}}{\partial x_{w,m}} & \frac{\partial x_{t,m}}{\partial y_{w,m}} \\ \frac{\partial y_{t,m}}{\partial x_{w,m}} & \frac{\partial y_{t,m}}{\partial y_{w,m}} \end{bmatrix} \quad (5.26)$$

the 2D Jacobian can be written as a function of $p_{w,m}$, $p_{p,m}$, a , and $y_m(a)$. After the derivative operations, the port position, $p_{p,m}$, is written as

$$\begin{bmatrix} x_{p,m} \\ y_{p,m} \end{bmatrix} = \begin{bmatrix} a \\ y_m(a) \end{bmatrix}. \quad (5.27)$$

Combining these equations with (3.10) permits calculation of the 2D Jacobian in terms of F_p , and a .

For infinitesimal motions orthogonal to the plane, I assume the instrument pivots about the port without changing shape. Such motions rotate the plane about a line that

passes through the port and that is orthogonal to the vector from wrist to tip. Therefore, infinitesimal orthogonal motions of either endpoint result in motions of the other endpoint that are also purely orthogonal to the plane. The scaling factor relating the magnitudes of the motions comes from the ratio of the instrument lengths on either side of the port. The resulting three-dimensional flexed instrument Jacobian is

$$J_i = R_m^{world} \begin{bmatrix} \frac{\partial x_{t,m}}{\partial x_{w,m}} & \frac{\partial x_{t,m}}{\partial y_{w,m}} & 0 \\ \frac{\partial y_{t,m}}{\partial x_{w,m}} & \frac{\partial y_{t,m}}{\partial y_{w,m}} & 0 \\ 0 & 0 & \frac{-(L-a)}{a} \end{bmatrix} (R_m^{world})^{-1} \quad (5.28)$$

$$R_m^{world} = [\hat{v}_x \quad \hat{v}_y \quad \hat{v}_z] \quad (5.29)$$

$$\frac{\partial x_{t,m}}{\partial x_{w,m}} = 1 + \frac{L}{L_{meas}^2} (y_m(a) + a\kappa) \sin(\varphi) \quad (5.30)$$

$$\frac{\partial x_{t,m}}{\partial y_{w,m}} = \frac{L}{L_{meas}^2} (-a + y_m(a)\kappa) \sin(\varphi) \quad (5.31)$$

$$\frac{\partial y_{t,m}}{\partial x_{w,m}} = \frac{L}{L_{meas}^2} (y_m(a) + a\kappa) \cos(\varphi) \quad (5.32)$$

$$\frac{\partial y_{t,m}}{\partial y_{w,m}} = 1 - \frac{L}{L_{meas}^2} (a - y_m(a)\kappa) \cos(\varphi) \quad (5.33)$$

$$\kappa = \frac{(2a - L - 1)y_m(a)}{a + (2a - L)y_m^2(a)} \quad (5.34)$$

$$L_{meas} = (a^2 + y_m^2(a))^{\frac{1}{2}} \quad (5.35)$$

5.2.6. Experimental Setup

In this teleoperation experiment, two desktop robots (Phantom Premium 1.5, Sensable Technologies; Woburn, MA) were used in a setup similar to minimally invasive

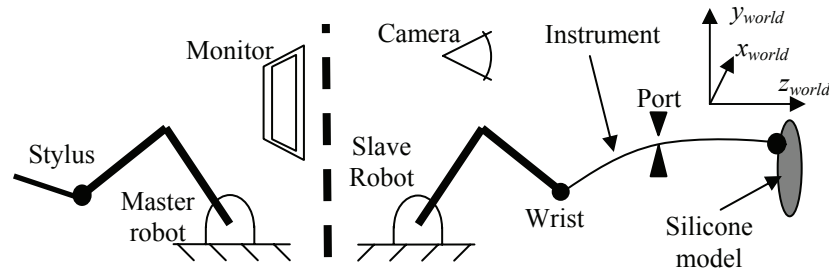


Figure 5.4. Diagram of experimental setup.

surgical robots (Fig. 5.4). The surgical site was modeled by a silicone rubber cylinder (RTV 6166, 3.4 kPa elastic modulus, General Electric; Fairfield, CT) held in a Petri dish (90 mm diameter, 15 mm deep) (Fig. 5.5). The Petri dish was held facing the “patient”-side robot at a distance of 740 mm from the robot.

The instrument was a stainless steel rod (600 mm long, 2.38 mm diameter), held by the patient-side robot. The rod passed through a port, consisting of a hole (2.49 mm diameter, 26 mm long) in a Teflon block, mounted to a gimbal placed 460 mm in front of the robot. Electromagnetic position and orientation sensors (Minibird, 800 Model, Ascension Technologies; Burlington, VT) were attached to the robot’s wrist, and 20 mm from the rod’s tip. Measurements from these sensors were made at 144 Hz and used in the controllers and flexion model. The measured RMS noise of the sensors was 0.13 mm and 0.00056 rad. Motor activity had no measurable effect on the readings for either sensor. When holding the desired tip position constant in the center of the task

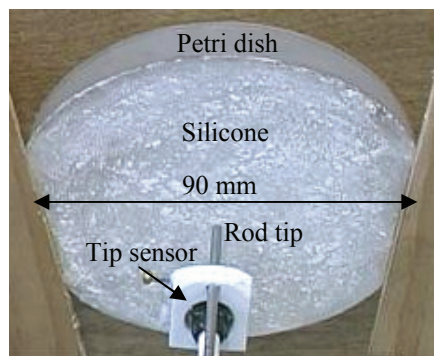


Figure 5.5. Camera view of silicone.

workspace, the RMS error in tip position was 0.16 mm for either of the controllers using tip tracking.

On the “surgeon” side, the subject moved the stylus attached to the master robot while watching a monitor. The monitor displayed a close-up view of the silicone and the tip of the rod. This view was recorded by a camera positioned 360 mm behind and 890 mm above the patient-side robot.

The desired position for the rod’s tip, $p_{t,desired}$, was set to the master robot’s position. This desired position was adjusted by a forbidden-region virtual fixture, a plane 6 mm into the silicone. Any desired tip positions deeper than this plane were projected onto the plane. The desired wrist position, $p_{w,desired}$, was calculated from this adjusted position using one of the four Jacobian-based controllers. The wrist was driven to this desired position using a proportional-derivative controller. No forces were exerted by the master robot.

5.2.7. Protocol

Subjects participated in a task motivated by image-guided minimally invasive blunt dissection. Image guidance took the form of a forbidden region virtual fixture designed to limit penetration depth of the rod’s tip into the silicone. Medical images can be used to position such virtual fixtures in relation to specific tissue locations. The robot controller then prevents the instrument from entering the areas protected by the virtual fixtures. As long as the robot’s controller is accurate, these limits prevent the instrument from interacting with the tissues at those locations, thereby increasing the patient’s safety. In this task, as the rod’s tip interacted with the silicone the rod flexed, changing the kinematic parameters. The various controllers’ performances are indicative of their

performances in any task involving quasi-static flexion, such as minimally invasive robotic surgery.

Subjects were instructed to move the master robot such that the rod's tip moved around in the silicone, staying within an outline drawn on the monitor. As the tip moved in the silicone, the silicone's surface was visibly damaged. Subjects were told to keep the tip inserted as deeply as possibly into the silicone, and to attempt to damage as much of the silicone within the outline as possible. Subjects were informed that a virtual wall would prevent the tip from entering the silicone too far. The outline drawn on the monitor corresponded to a 40 mm diameter circle on the silicone and was meant to keep the rod's tip away from the sides of the Petri dish.

Subjects were graduate students, with ages between 21 and 30, mean age 26 years. Before the actual trials, twelve minutes of training time were allowed, divided into three minutes for each of the Jacobian-based controllers. After the training, subjects performed a one minute trial for each controller, in the same order as the training. Between controllers, subjects were allowed to pause and stretch, and the silicone model was replaced. Ten subjects participated in this experiment, and the order of the controllers was counterbalanced between subjects. The position measurements from the magnetic tracker at the rod's tip were recorded during the trials.

5.3. Results

For all subjects, the controller with both tip tracking and improved kinematics incurred least into the forbidden region (Fig. 5.6). Meanwhile, the controllers with either tip tracking or improved kinematics incurred less often and less deeply than the controller

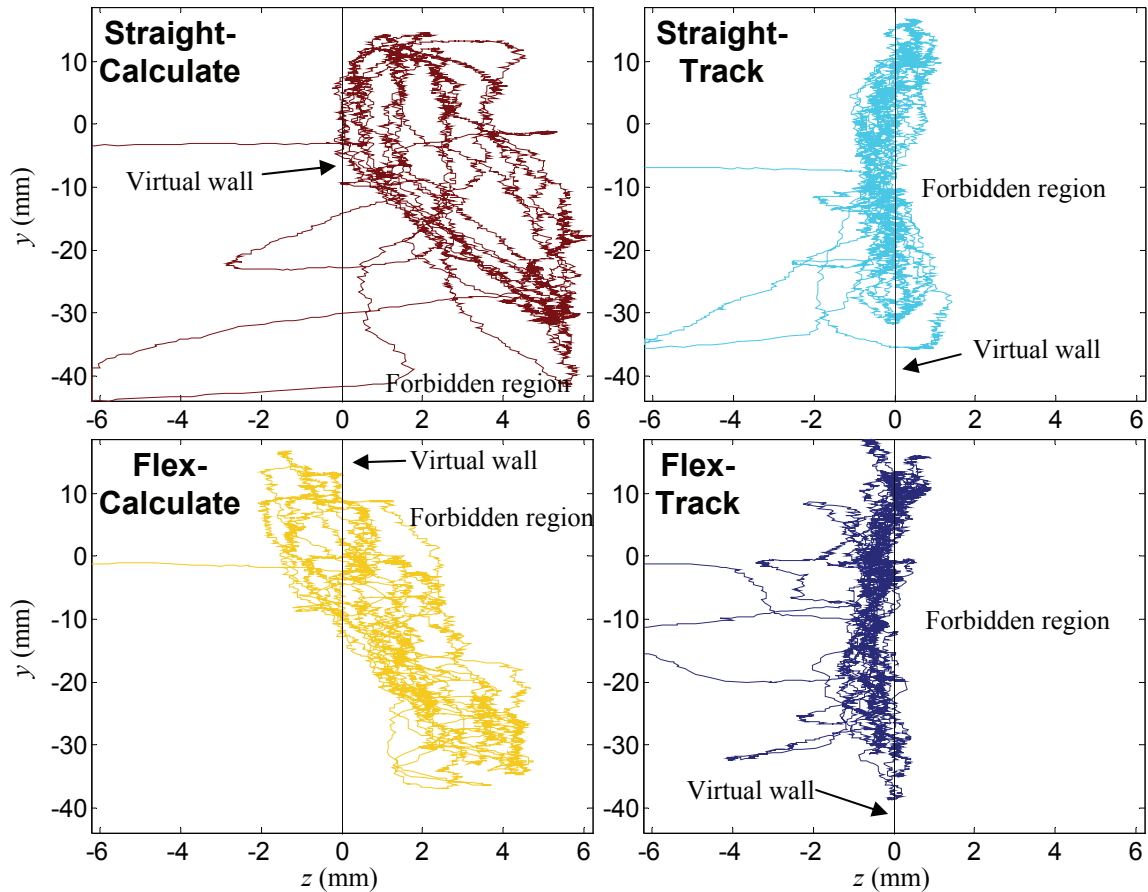


Figure 5.6. Tip trajectories from the subject with the median maximum incursion depths, projected into the vertical plane. Flex-Track enters the forbidden region the least, followed by Straight-Track and then Flex-Calculate. Axes use different scaling to show detail.

with neither. By examining the average time each controller spent at various depths, the benefits of both tip tracking and more accurate kinematics are clear (Fig. 5.7).

The percentage of time each controller spent within the forbidden region was (mean \pm standard deviation): Flex-Track $11\% \pm 5\%$, Straight-Track $32\% \pm 10\%$, Flex-Calculate $59\% \pm 13\%$, and Straight-Calculate $78\% \pm 10\%$. Using Student's t-tests to compare each mean with respect to each other mean, all differences are significant at $p \leq 0.002$. The maximum depth each controller incurred into the forbidden region was: Flex-Track $1.0 \text{ mm} \pm 0.5 \text{ mm}$, Straight-Track $2.0 \text{ mm} \pm 1.0 \text{ mm}$, Flex-Calculate $4.3 \text{ mm} \pm 1.0 \text{ mm}$, and Straight-Calculate $6.0 \text{ mm} \pm 0.5 \text{ mm}$ ($p \leq 0.011$), (Fig. 5.8).

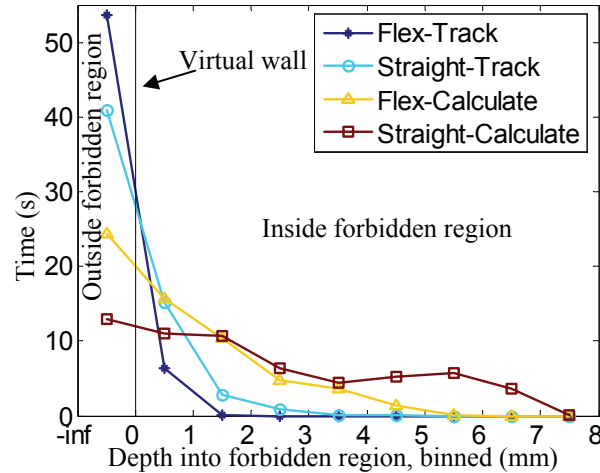


Figure 5.7. Histogram of average time spent at various incursion depths. Straight-Calculate spends the most time inside the forbidden region, and has the deepest incursions.

The damage to the silicone inside the forbidden region was estimated in two ways. First, the trapezoidal rule was used to estimate the area between the virtual wall and pairs of temporally adjacent tip positions within the forbidden region. Averaged across subjects, these areas are: Flex-Track $39 \text{ mm}^2 \pm 21 \text{ mm}^2$, Straight-Track $320 \text{ mm}^2 \pm 330 \text{ mm}^2$, Flex-Calculate $1500 \text{ mm}^2 \pm 610 \text{ mm}^2$, and Straight-Calculate $3400 \text{ mm}^2 \pm 1100 \text{ mm}^2$ ($p \leq 0.013$). Then, to prevent counting damage to the same piece of silicone more

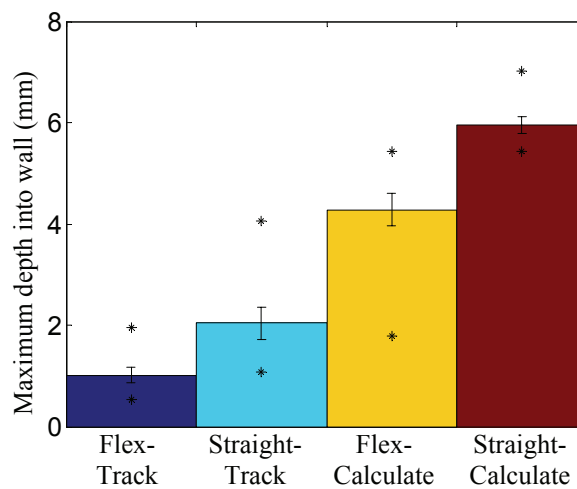


Figure 5.8. Depth of maximum incursions per controller, averaged across all subjects. Lines show one standard error in either direction. Asterisks show minimum and maximum. All means significantly different at $p \leq 0.011$.

than once, the trajectories were projected onto two planes orthogonal to the virtual wall and to each other. For each of the two planes, the area within the outline of the projection was calculated. The two areas were summed together, and the averages across subjects are: Flex-Track $15 \text{ mm}^2 \pm 10 \text{ mm}^2$, Straight-Track $86 \text{ mm}^2 \pm 81 \text{ mm}^2$, Flex-Calculate $230 \text{ mm}^2 \pm 86 \text{ mm}^2$, and Straight-Calculate $352 \text{ mm}^2 \pm 86 \text{ mm}^2$ ($p \leq 0.014$), (Fig. 5.9).

5.4. Discussion

Both tip tracking and the flexed instrument model improved the motion accuracy of image-guided teleoperation involving a flexing instrument. Compared with the controller using neither improvement, average reductions in the maximum incursion depth and the outlines of damaged area inside the forbidden region were 28% and 35% for flexed rod kinematics, 67% and 76% for tip tracking, and 83% and 96% for the combination of tip tracking and improved kinematics. Both improvements are highly advantageous for any control task that involves quasi-static flexion and requires high accuracy, such as image-

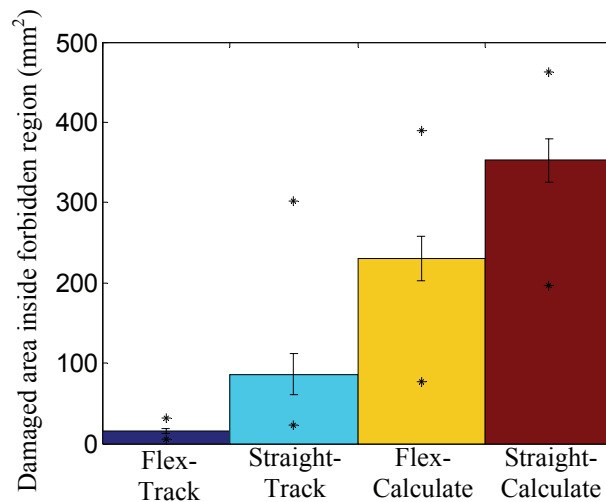


Figure 5.9. Area calculated from union of trajectories projected onto orthogonal planes, averaged across all subjects. Lines show one standard error in either direction. Asterisks show minimum and maximum. All means significantly different at $p \leq 0.014$.

guided robotic surgery.

Tip tracking provided the largest reduction in the erroneous motions. The performance of surgical robots can therefore be significantly improved by just measuring the position of the instrument tip using electromagnetic sensors or computer vision. The magnitude of improvement will be dependent on the sensor's accuracy, noise characteristics, and susceptibility to target occlusion.

The controller with flexion kinematics but not tip tracking performed better than the controller with neither improvement, but not as well as either controller with tip tracking. Its performance enhancement comes from improvements in the calculations of both the Jacobian and the tip position. These improvements are dependent on three factors: the agreement between the form of the model and the actual shaft geometries, the accuracy of the fit model parameters, and the registration accuracy between model coordinates and world coordinates. Like the benefits of tip tracking, these last two factors are dependent on the sensor capabilities. Even more than tip tracking, the parameter fit and registration are sensitive to sensor noise, e.g., small errors in wrist angle lead to large tip errors at the end of a long rod. As sensors improve, errors in the calculated tip position will decrease, closing the gap between this controller and the controllers with tip tracking. At some level of sensor accuracy and precision, the controller with flexion kinematics but not tip tracking may perform better than the controller with straight shaft kinematics and tip tracking.

The proposed model requires just two measurements to fit instrument flexion resulting from forces orthogonal to the instrument at the wrist, cannula, and tip. From the measurements, the instrument shape is modeled and the port position is determined. The

forces used in the model were identified by observation during surgery as being the biggest cause of tip deflection. A more general flexion model would include instrument buckling due to axial forces, distributed forces caused by tissue interactions along the instrument, and a moment at the cannula caused by the insertion site resisting cannula rotation. Experiments in the operating room will be necessary to evaluate the need for more complicated models that address such flexion sources. Additional sensors would be needed to fit the increased number of parameters, or could be used to reduce a simpler model's sensitivity to measurement noise.

The amount of information in a sensor modality affects the choice of controller. Current commercial electromagnetic sensors provide enough information to both track the instrument tip and to fit the flexion model, therefore the controller with both tip tracking and flexion modeling can be used to maximize performance. The controllers with just tip tracking or just flexed rod kinematics are important because other sensing methodologies can provide only enough information for one enhancement or the other. For example, force sensors at the wrist and tip could provide measurements for fitting the flexion model's parameters, but cannot directly measure the tip position. Conversely, computer vision techniques could localize the tip position, but may not be able to measure the endpoint orientation with sufficient accuracy to fit the model parameters.

During the experiment, the silicone generated forces to resist motions of the instrument tip. Preliminary trials investigated several materials, including four different elastic moduli of silicone rubber and two different viscous clays. In those investigations, the material had little effect on the performance benefits observed between the four controllers. Silicone was used for this experiment because it is easily characterized and

duplicated. The silicone's elastic modulus was relatively soft (3.4 kPa) because hard silicones tended to fracture, causing dynamic oscillations as energy stored in the flexed instrument was released. The experimental results are a function of the instrument flexion, so the model's material is relatively insignificant as long as quasi-static instrument flexion occurs.

The best-performing controller in this experiment still entered the forbidden region due to measurement noise, model assumptions (e.g., no buckling from axial forces), and shape changes between controller updates, which was limited to 144 Hz for the sensor used here. For a controller to follow the boundary of the forbidden region without entering it, either the update rate would have to be much faster, or the environmental response to a desired tip motion would have to be modeled. Without such modeling, interaction forces can unexpectedly alter the shape of the instrument between controller updates and cause the instrument to enter the forbidden region.

The results of this experiment demonstrate the benefits of tip tracking and model-based error correction on accurate positioning in the presence of quasi-static flexion. Without these benefits, image-guidance is hampered by errors in instrument motions, and in the calculated instrument tip position. With these benefits, techniques such as virtual fixtures and augmented reality can accurately guide the surgeon.

Chapter 6

Conclusion and Future Work

Surgical robots can increase the safety and reduce the duration of surgeries, but their full potential is prohibited by kinematic errors. Specifically, the erroneous assumptions of a straight instrument and a stationary insertion point have caused failure in previous attempts to protect delicate tissues using image-guided surgical robots. This research investigated methods to quantify and reduce the impact of those kinematic errors. The three major results of this dissertation are quantification of motion errors caused by incorrect kinematics, a model of the kinematics for a flexed instrument, and a demonstration of the image-guidance benefits from tip tracking.

6.1. Evaluation of motion errors

The presented research demonstrated several ways in which controllers that do not account for instrument flexion lead to errors in the motions of surgical instruments. First, simulations showed that small errors in port localization are sufficient to cause divergent tip motions near workspace boundaries, even with tip tracking (Chapter 2). Then, experiments with instrument flexion from indenting a silicone block showed path deviations greater than 10% of the desired motion length (Chapter 4). Finally, in a

teleoperation study, subjects using a controller that did not account for flexion spent 80% of the trial time inside the forbidden region virtual fixture, and penetrated up to 6 mm into the region on average (Chapter 5). Additionally, a metric was described that quantifies the worst-case convergence rate of controllers with bounded kinematic errors.

6.2. Image-guidance benefits from tip tracking

Measuring the position of the instrument's tip is a straight-forward response to incorrect forward kinematics. Combining tip tracking with a controller based on relative motions, such as a Jacobian-based controller, makes the tip converge to the desired position even in the presence of small kinematic errors. This capability was demonstrated most clearly in the dynamic indentation trials in Chapter 4, and is why the controllers evaluated by the metric presented in Chapter 2 can converge to the desired position even while using incorrect kinematics. This benefit of tip tracking exists regardless of the type of kinematic error, although convergence may not occur for kinematic errors of a significant magnitude.

In the user study, the benefit of tip tracking was investigated separately from the benefit from improved kinematics. Adding tip tracking reduced the maximum penetration depths into the forbidden region virtual fixture by approximately 70%, with or without the improved kinematics. For the Jacobian using the kinematics from a straight instrument, adding tip tracking to the controller halved the time spent in the forbidden region and reduced the area damaged by 75%.

The sensing modalities most feasible for localizing the instrument's tip during surgery are electromagnetic sensors and the laparoscope. Commercial electromagnetic sensors are small enough to fit inside surgical instruments and do not suffer from line-of-

sight occlusions, but their accuracy is dependent on being spatially separated from metal and varying magnetic fields. Alternatively, the tip position can be determined by using computer vision techniques on the laparoscopic image. This approach has relatively reduced mechanical complexity, but suffers from the possibility that the tip will be occluded by another instrument or the environment. The viability of the two localization methods need to be evaluated in actual surgical procedures.

6.3. Kinematic modeling

A kinematic model for flexing instruments was proposed and then investigated in simulation and experiments. The model addresses the two kinematic errors observed to have the largest impact on instrument shape: instrument flexion and port localization. The kinematics provided by the model were demonstrated to be a significant improvement over the assumption of a straight instrument through quasi-static simulations and experiments. The teleoperation trials validated the model by using forces caused by interactions at the instrument tip, a situation similar to robotic surgery. Instrument flexion will become more pronounced as surgeons seek to minimize instrument size to reduce damage to healthy tissue and access smaller anatomical structures. The accuracy benefit provided by the presented model will consequently increase.

The error sources addressed by the presented model were chosen through observations of robotic surgery and discussions with surgeons. To evaluate the kinematic accuracy of the model, kinematic changes would need to be recorded during an actual surgery. Such recordings would allow evaluation of additional sources of kinematic error. Two error sources not addressed by the presented model are a moment at the port from the incision resisting port rotation, and forces distributed along the instrument from

interactions with the surgical environment. To fit a model addressing more sources of kinematic error, more measurements would be needed. The best possible setup for accurate kinematics may be intraoperative imaging from Magnetic Resonance Imaging (MRI), 3D Ultrasound, or a CAT scanner. Throughout the procedure, the imaging system would provide three-dimensional images containing both the instrument shaft and the surgical site.

As the accuracy of the kinematic model increases, the additional benefit provided by tip tracking decreases. This relationship is important when considering alternative sensor modalities for fitting the model parameters. For example, several strain gages bonded along the instrument may provide enough low-noise measurements that the kinematic model could determine the tip position with high accuracy when combined with precise measurements of the position and orientation of the robot's wrist.

6.4. Future work

Image-guided robotic surgery relies on accurate knowledge of the instrument position and the ability to move the instrument directly to desired positions. This work has investigated the effects of changing instrument shaft kinematics on those two factors, and has provided means to improve performance. The proposed model does not address other kinematic errors. In particular, the commercial system that prompted this work, the Zeus surgical robot system, exhibits significant joint and link compliance as well as actuator backlash. This work assumes those properties are addressed by the built-in joint level controller, as none of them are addressed by the model. From my experience, the tip deflection resulting from joint and link compliance are on the order of the deflection from instrument flexion. Similarly, the motion errors due to kinematic errors in the arm would

likely be equivalent to those from the instrument shaft. As a result, I would expect the system to continue to display motion errors, even when using the proposed controller. These motion errors would be reduced with the use of tip tracking and should be small enough to allow beneficial image guidance techniques. Other surgical robots may not have such issues, depending on construction.

This work did not explore safety issues, an important factor in robotic surgery. The proposed controller was shown to reduce motion errors in a controlled environment. In the operating room, electromagnetic sensors may suffer from increased noise due to interference from monitors, radio-frequency instruments, and high-power lines running through the walls. Since I did not perform experiments using an actual surgical instrument in the operating room, nor did I investigate noise-reduction improvements in the sensors I used, it is unclear if the proposed controller would perform better than a straight shaft controller in surgery. Tip tracking significantly improved performance in a controlled environment, but if the tip sensor suffered from significant noise for even a fraction of a second, the robot would move to reduce that position “error.” Of course, high frequency noise can be reduced with a low pass filter, but at the cost of responsiveness. Similarly, if computer vision techniques were used to localize the tip position, occlusions would be a significant problem. Occlusions have been addressed in visual servoing literature, but possibly not sufficiently for use in surgery. Sensors for tip tracking and calculating the model parameters may not be robust enough to implement the proposed controller in the operating room.

Further questions are concerned with the specific surgical applications of image-guidance or autonomous instrument motions. The benefit of image guidance is a function

of surgery-specific factors such as the structure of the surgical site, the surgical difficulty, and the degree of anatomical change between the imaging and the end of the surgery. Future work will address which surgeries are most helped by image guidance, and how best to use images to guide instrument motions.

References

- [Abbott 03] J. J. Abbott and A. M. Okamura, "Virtual Fixture Architectures for Telemanipulation," *IEEE International Conference on Robotics and Automation*, pp. 2798-2805, 2003.
- [Belendez 02] T. Belendez, C. Neipp, and A. Belendez, "Large and small deflections of a cantilever beam," *Eur. J. Phys.*, 23:371-379, 2002.
- [Cheah 03] C. C. Cheah, M. Hirano, S. Kawamura, and S. Arimoto, "Approximate Jacobian control for robots with uncertain kinematics and dynamics," *IEEE Trans. Robotics and Automation*, 19(4):692-702, 2003.
- [Coste-Maniere 04] E. Coste-Maniere, L. Adhami, F. Mourgues, and O. Bantiche, "Optimal planning of robotically assisted heart surgery: first results on the transfer precision in the operating room," *Intl. J. of Robotics Research*, 23(4-5):539-48, 2004.
- [Falk 99] V. Falk, J. McLoughin, G. Guthart, J. K. Salisbury Jr, T. Walther, J. Gummert, and F. W. Mohr. "Dexterity enhancement in endoscopic surgery by a computer controlled mechanical wrist." *Minimally Invasive Thoracic and Allied Technology*, 8(4):235-242, 1999.
- [Fung 93] Y. C. Fung. *Biomechanics: Mechanical Properties of Living Tissues*. Springer-Verlag, New York, New York, 1993.
- [Grimson 98] W.E.L. Grimson, M. Leventon, G. Ettinger, A. Chabrierie, F. Ozlen, S. Nakajima, H. Atsumi, R. Kikinis, and P. Black. *Clinical experience with a high precision image-guided neurosurgery system*. Springer-Verlag, Boston, Mass., 1998.
- [Guthart 00] G. Guthart and K. Salisbury, Jr., "The Intuitive™ telesurgery system: overview and application," *IEEE Intl. Conf. on Robotics and Automation*, pp. 618-621, 2000.
- [Hills 98] J. W. Hills and J. F. Jensen. "Telepresence technology in medicine: principles and applications." *Proceedings of the IEEE*, 86(3):569-580, 1998.
- [Hollerbach 96] J. M. Hollerbach and C. W. Wampler, "The calibration index and taxonomy for robot kinematic calibration methods," *Intl. J. of Robotics Research*, 15(6):573-591, 1996.
- [Hosoda 94] K. Hosoda and M. Asada, "Versatile visual servoing without knowledge of true Jacobian," *Intl. Conf. on Intelligent Robots and Systems*, pp. 186-193, 1994.
- [Hutchinson 96] S. Hutchinson, G. Hager, and P. Corke. "A Tutorial Introduction to Visual Servo Control," *IEEE Transactions on Robotics and Automation*, 12(5):651-670, 1996
- [Jägersand 96] M. Jägersand, "Visual servoing using trust region methods and estimation of the full coupled visual-motor Jacobian" *IASTED Applications of Robotics and Control*, pp. 105-108, 1996.
- [Kwon 94] D.-S. Kwon and W. J. Book, "A time-domain inverse dynamic tracking control of a single-link flexible manipulator," *J. of Dynamic Systems, Measurement, and Control*, 116:193-200, 1994.
- [Lardner 94] T. J. Lardner and R. R. Archer. *Mechanics of solids: an introduction*. McGraw-Hill, New York, 1994.

- [Marayong 03] P. Marayong, M. Li, A. M. Okamura, and G. D. Hager, "Spatial Motion Constraints: Theory and Demonstrations for Robot Guidance using Virtual Fixtures," *IEEE International Conference on Robotics and Automation*, pp. 1954-1959, 2003.
- [Panait 02] L. Panait, C. Doarn, and R. Merrell, "Applications of robotics in surgery," *Chirurgia Bucuresti*, vol. 97, no. 6, pp. 549-55, 2002.
- [Park 01] S. S. Park, R. D. Howe, and D. F. Torchiana, "Virtual fixtures for robot-assisted minimally-invasive cardiac surgery," *Medical Image Computing and Computer-Assisted Intervention 2001*, W.J. Niessen and M.A. Viergever, Eds. Berlin: Springer-Verlag, Berlin, 2001, pp. 1419-1420.
- [Piepmeier 99] J. A. Piepmeier, G. V. McMurray, and H. Lipkin. "A dynamic quasi-newton method for uncalibrated visual servoing," *IEEE International Conference on Robotics and Automation*, pp. 1595-1600, 1999.
- [Peters 00] T. M. Peters, "Image-guided surgery: from X-rays to virtual reality," *Computer Methods in Biomechanics and Biomedical Engineering*, vol. 4, pp. 27-57, 2000.
- [Roth 87] Z. Roth, B. W. Mooring, B. Ravani, "An overview of robot calibration," *IEEE Trans. Robotics and Automation*, 3(5):377-385, 1987.
- [Rovner 87] D. M. Rovner and R. H. Cannon, Jr., "Experiments toward on-line identification and control of a very flexible one-link manipulator," *Intl. J. of Robotics Research*, 6(4):3-19, 1987.